Pathways for Mechanotransduction in Pressurized Airway Epithelial Cells

by

Anna K. McVittie

B.S., Mechanical Engineering
Stanford University, 1999

Submitted to the Mechanical Engineering Department,
In Partial Fulfillment of the Requirements for the Degree of
Master of Science in Mechanical Engineering

at the

Massachusetts Institute of Technology

February 2001

Signature of Author.....
Department of Mechanical Engineering
February 8, 2001

Certified by.....
Roger D. Kamm
Professor of Mechanical Engineering and
Bioengineering and Environmental Health
Thesis Supervisor

Accepted by.....
Ain A. Sonin
Chairman, Department Committee on Graduate Students

Pathways for Mechanotransduction in
Pressurized Airway Epithelial Cells

by

Anna K. McVittie

Submitted to the Department of Mechanical Engineering
on February 8th, 2001 in Partial Fulfillment of the
Requirements for the Degree of Master of Science in
Mechanical Engineering

ABSTRACT

A study was performed to determine pathways for mechanotransduction in pressurized airway epithelial cells. In asthmatic airways, thickening of the airway walls leads to altered buckling patterns that apply a substantial normal force to the surface epithelial cells. This compressive force may contribute to airway wall remodeling and the pathogenesis of asthma.

Previous studies have shown that a transepithelial pressure difference of 30 cmH_2O caused the upregulation and activation of certain genes and proteins that are implicated in airway wall remodeling.

In this study, cell culture tests, finite element models, TEM, and two-photon microscopy were combined to study how a trancellular pressure difference leads to a biological response. Cell cultures were used to determine what signaling cascades are activated due to a pressure difference and to an osmotic shock. Finite element models were created to determine the magnitude and distribution of stresses associated with a variety of mechanical events that could be important in pressurized cells. Finally, TEM and two-photon microscopy provided images of the cell layer morphology before, during, and after pressure application.

Cell culture results show activation of specific signaling pathways in response to a trancellular pressure. The finite element models indicate increased stresses in the cytoskeleton, nucleus, and membrane in response to bead twisting, to pressurizing a cell layer on a porous substrate, and to pressure induced collapse of the lateral intercellular spaces. Imaging results showed increased pooling in the intercellular spaces of the airway epithelial cells while exposed to a trancellular pressure difference.

This thesis provides useful insight into the response of epithelial cells to a trancellular pressure difference and suggests a number of different pathways that may play a role in mechanotransduction in asthmatic airways.

Thesis Supervisor: Roger D. Kamm
Title: Professor of Mechanical Engineering and of Bioengineering and Environmental Health

Acknowledgements

There are few times in our lives when we get to go back and thank the people that are influential in our lives and in the milestones we achieve along the way. This thesis project and my time at MIT was both a great academic and personal achievement and there are a number of people whom I would like to thank.

First and foremost I would like to thank Prof. Roger Kamm for letting me take over a project that one of his best PhD students, Barbara Ressler, had been working on. He started me off by opening all the doors and then he let me have a large say as to which paths I chose. Admittedly, I was incredibly overwhelmed when I first started, but slowly and surely different paths started to take root and I was able grasp what this research project was all about. Prof. Kamm gave me great advice and challenged me to understand the hows and whys of everything I did.

Post-doctoral fellow Dan Tschumperlin guided me throughout this thesis project, always giving me good advice and suggestions. Dan also did a large part of the of the cell culture work for which I am grateful. Jon Shively played an instrumental role in providing my cells for imaging and all my last minute dextran packages. I'd also like to thank Dr. Jeffrey Drazen for his counsel and funding.

Prof. Peter So gave me guidance and advice as well as access to the two-photon imaging system. Lily Hsu devoted hours throughout many days and nights helping me with the two-photon microscope when she still had her own work to do. I'm also grateful for Rebecca Sterns who helped me with the TEM imaging.

Leslie Regan and Claire Sasahara deserve much gratitude for their kindness, advice, and plethora of information.

I would also like to acknowledge everyone in the fluids lab who provided me with entertainment, advice, encouragement, and help. Most importantly, Ana Isasi, who let me take over her computer, and who was a kind friend. One of the hardest parts about leaving MIT is leaving the kind and generous people I was fortunate to interact with on a daily basis.

Besides all the people who helped on the research side, many others contributed to making my time at MIT and in Boston, very enjoyable. They include, John W. and all the BEH folks, the Canadians and all the aero-astros, Alexis, Brigitte, my Stanford friends, my new and old roommates, and many others. I'd especially like to thank Jon Szafranski who helps me keep my life in perspective and who always provides a shoulder to lean on.

Most of all I'd like to thank my family, in particular my parents. Their encouragement and support help me through thick and thin, and their love for knowledge, and diligent and honest work ethic, provide an example that I strive to match.

Table of Contents

List of Figures

List of Tables

Chapter 1
Introduction

Epithelial cells adapt and respond to their complex biological surrounding. They are constantly sending and receiving mechanical, biological, and chemical signals to perform certain functions. Recently, there has been an increased attempt to determine the role of mechanical forces on the cellular level in disease initiation and progression. The process by which an applied force initiates a biological signal leading to a sequence of events inside and outside the cell is termed "mechanotransduction". Much research has focused on stresses and conformational changes in the cell and in cell attachments that could initiate a biological response.

Cells in their natural environment encounter many mechanical signals. Some mechanical stimuli that have received considerable attention are increased fluid flow, pressure, and substrate strain during pathological situations. In this study we investigated possible mechanotransduction pathways in airway epithelial cells exposed to a transcellular pressure difference that could contribute to remodeling events seen in asthmatic airways. Our methods combine finite element modeling with cell culture studies and imaging techniques in a novel way to understand the multifaceted environment in which airway epithelial cells live.

1.1 Asthma

Asthma is a chronic inflammatory disease of the airways that afflicts approximately 15 million people in the United States. While the features of asthma have been extensively studied, the underlying cause and the progression of the disease are still not fully understood.

Asthma is characterized by hyperresponsive airways that constrict more readily than normal airways when exposed to various pathogens. The initiating factors were originally thought to be abnormal smooth muscle cells and an increased cholergenic response (10) that caused the airways to respond more quickly and with a higher degree of force. It was later determined that inflammation plays a central role in the progression and symptoms of the disease. Inflammation is caused and sustained by the infiltration of a variety of primary effector cells, such as lymphocytes (34), eosinophils (62), and mast

cells (44) that can contribute to smooth muscle constriction and epithelial cell damage (10).

Recently more attention has focused on the remodeling or structural changes that occur in asthma. Asthmatic airways undergo various changes including increased mucus production, myocyte hyperpalasia and hypertropy, and epithelial hypertrophy (10). All these, in addition to the deposition of collagen and other matrix proteins beneath the basement membrane, increase the thickness of all layers of the airway wall (22).

Subepithelial thickening has been shown to alter the constriction pattern in the airways thereby causing the epithelium to buckle into deep crevasses (64). Figure 1.1A shows the cross-section of a normal human airway with many small folds. Figure 1.1B shows an asthmatic airway with increased wall thickness and fewer folds. The altered buckling pattern accompanying increased wall thickness significantly increases the stresses epithelial cells experience (61). When the airway walls fold into deep crevasses, the epithelial cells lining the surface are pushed up against each other, exposing the apical surface of the epithelial cells to a substantial normal force (Figure 1.2). It is this force, among other factors, that may contribute to airway wall remodeling independent of inflammatory factors.

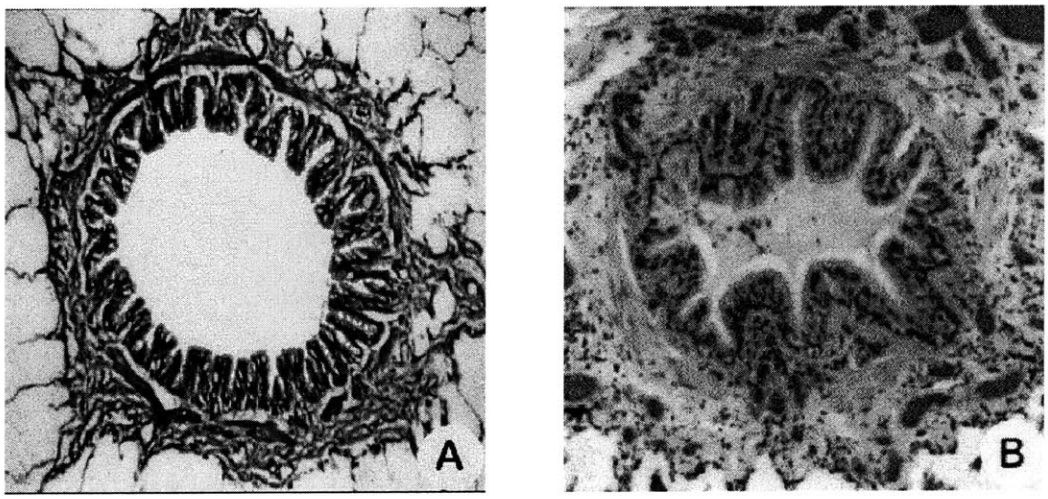

Figure 1.1: A)Normal and B)asthmatic human airways during smooth muscle constriction (From UBC PRL.).

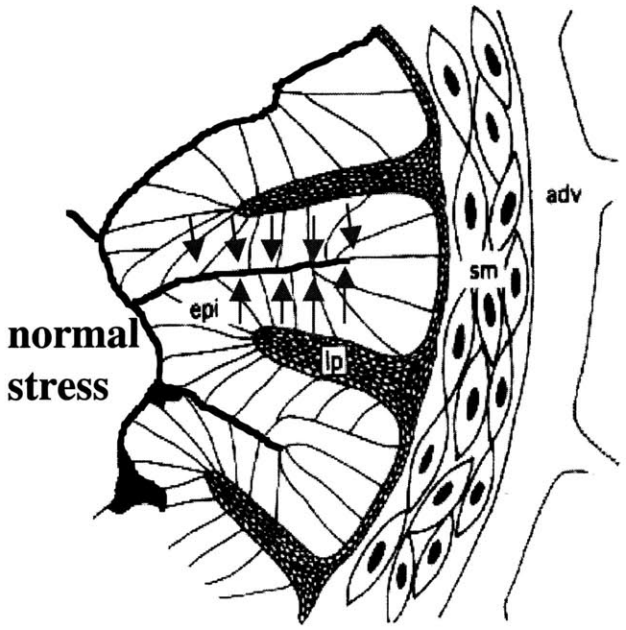

Figure 2: Highly constricted guinea pig airway. (Yager et al., 1996)

During normal inspiration and expiration, the epithelial cells are exposed to pressures that seldom exceed 1 cmH_2O (60). When smooth muscle constriction causes the airway walls to buckle, increased compressive stresses applied to the surface epithelium are in excess of 30 cmH_20 (16). Exposure of the epithelium to a considerably higher degree of compressive stress than during normal conditions may lead to airway remodeling.

Recently, Ressler, et al, showed that *in vitro* cells respond to compressive stress in the form of an applied transcellular pressure difference by upregulating the expression of certain genes leading to protein synthesis that are known to play a role in airway wall remodeling. The genes investigated are known to increase extracellular matrix (ECM) deposition and smooth muscle cell (SMC) contraction (37). In particular, early growth response-1 (Egr-1) and transforming growth factor beta (TGF-β) increased in response to a transcellular pressure difference ranging from 2 to 20 cmH_2O. Egr-1 activates platelet derived growth factor (PDGF; 24), which has been shown to increase fibroblast proliferation and collagen deposition (36). TGF-β aids in fibrosis by increasing fibronectin and collagen genes in fibroblasts. Ressler showed that Egr-1 and TGF-β

increase in a time and pressure dependent manner and concluded that a transepithelial pressure has a direct effect on the biological response of airway epithelial cells.

It is crucial to the treatment of any disease to understand the role of mechanical forces and the pathways by which complex stresses can lead to a biological response that contributes to the disease progression. The mechanical forces cells experience, and the means by which the forces elicit a biological response, are complex and require insight into the mechanical properties of the cell itself. Previous studies have attempted to characterize cell mechanics and the role it plays in mechanotransduction.

1.2 Mechanisms of Force Transmission and Mechanotransduction

1.2.1 The Role of the Cytoskeleton

The cytoskeleton (CSK) is thought to play an important role in signal transduction. It has been shown to remodel in response to fluid flow (40) and to changes in cell-cell or cell-substrate attachments (35). Satcher et al. (40) used freeze-fracture techniques to show cytoskeletal connections between the apical and basal surfaces and in the cell interior up to the nucleus. The compression/tension modulus of the distributed cytoplasmic structural actin network (DCSA) was calculated to be $2x10^5$ dyn/cm^2. Filaments were also found bridging between cell membranes in the intercellular gap. These filaments were 8 nm in width, 50 nm long, and spaced ~25 nm apart.

A variety of techniques have been used to quantify the material properties of the cytoskeleton. Using a micropipette technique the Young's Modulus was found to be in the range of 10^2-10^3 Pa (55), and in a magnetic cytometry experiment the Young's Modulus of the cytoskeleton was determined to be on the order of 10-10^2 Pa (57)

As the primary stress-bearing component within a cell, the cytoskeleton could potentially transmit forces from the membrane to the nucleus and thus act as a signaling pathway for mechanical forces (57). Previous investigators (56) have proposed an integrated "tensegrity" model in which the cytoskeleton is composed of independent struts in tension and others in compression. Due to the interconnected nature of the cytoskeleton, perturbing even one strut causes a rearrangement of the network.

1.2.2 Integrins

At the level of the membrane integrins connecting the ECM to the CSK are thought to play a key role in the transfer of forces between the ECM and the CSK. Integrins are transmembrane cell adhesion molecules that participate in cell–matrix interactions. Inside the cell, integrins are bound to adaptor proteins, such as vinculin, (29) which attach to the cytoskeleton. Because they are directly attached to the cytoskeleton, integrins transmit mechanical stresses from the outside environment to the cytoskeleton where structural rearrangement occurs. Therefore, in a tensegrity model, localized stress arising from magnetic beads attached to integrins may cause a global change throughout the cytoskeleton that can act to induce biological changes.

Magnetic cytometry, also known as bead twisting, exploits the role of integrins in force transmission from the ECM to the CSK. Magnetic twisting cytometry has been implemented to understand cytoskeletal mechanics in confluent epithelial cells (Tschumperlin, unpublished results). Potard, et al.(35), used 4 μm ferromagnetic beads coated with ligands for specific surface epithelial integrins to study CSK-ECM coupling. The cells were placed in a magnetic twisting cytometer, which uses a magnetic field to cause the beads to rotate. The twisting applies a shear stress directly to the cytoskeleton via integrins. Stresses arising from the twisting bead caused an increase in cytoskeleton stiffness as measured by the ratio of stress (torque-volume) to angular strain (rotation) at the end of 1-minute twist. When the microtubules or microfilaments were destroyed the increase in cytoskeleton stiffness was greatly reduced.

In an experiment performed by Wang and Ingber (57), referred to previously, ferromagnetic beads with a specific RGD coating were attached to endothelial cells and then placed in a magnetic twisting device that caused the beads to rotate. The study concluded that bead twisting caused alterations in cytoskeleton stiffness and viscosity through integrins molecularly linked to the cytoskeleton.

1.2.2 Mechanical Stimuli

Many mechanical stimuli have been shown to initiate biological responses in cell systems. Substrate strain, osmotic challenge, pressure, shear stress, and localized

deformations are all mechanical events that have elicited biological responses in certain epithelial cell systems. Each pathway is further expounded upon in the following sections. It should be noted however, that the observed biological response is likely a synergistic effect arising from a number of mechanisms.

1.2.2.1 Strain

Strain is a mechanical stimulus used in a number of experiments. For example, cyclic substrate strain stimulates endothelial cells to proliferate (52), causes membrane hyperpolarization in chondrocytes (28), and increases the release of calcium in airway epithelial cells (12). Substrate strain also caused deformations in the cell nucleus suggesting that the nucleus can directly sense mechanical changes in the cytoskeleton (4). Stretch-activated channels which may respond to membrane strain have been found on the basolateral walls of airway epithelia (25).

1.2.2.2 Osmotic Shock

Osmotic shock is known to elicit a biological response on many cell types. Reuss et al (39) showed that hyposmotic swelling activates ion channels through stretch causing membrane hyperpolarization and a subsequent decrease in cell volume. Hypertonic stress has also been shown to activate mitogen activated protein kinases (MAPK, 20) that lead to increased production of certain proteins in the nucleus.

1.2.2.3 Shear Stress

The effects of increased shear stress due to fluid flow on cell systems have been studied extensively. Dewey et al. (9) showed that a shear stress of 8 dyn/cm^2 applied to the apical surface of endothelial cells caused the cells to elongate and realign. Shear stress caused the cytoskeleton to undergo significant reorganization and a change in shear rate caused the rate of endocytosis to double from that at a steady shear rate (8). In both endothelial and epithelial cells exposed to a fluid shear stress of 5 dyn/cm^2, Egr-1 was activated through the ERK1/2, MAPK pathway (44). Takahaski also showed that MAP kinases ERK1/2 and p44/42 are activated in vascular endothelial cells exposed to shear stress (53).

There is evidence that shear stress acts to activate specific MAP kinases through β1 integrin activation (19). However, the increase in ERK caused by shear stress was greater than the response due to integrin activation alone, suggesting that integrin activation is only one of the mechanosensory events involved.

Though less extensively studied, shear stress caused by fluid flow can also act in the lateral intercellular space (LIS) along the basolateral membrane of epithelial cells. While the method by which transport occurs is still in dispute, Spring summarized the possible pathways for fluid transport in glandular epithelial cells (48). These include paracellular (between the cells, Figure 1.3A), transcellular (through the cells), and transcellular and then paracellular fluid transport pathways (Figure 1.3B). A standing gradient model was originally hypothesized whereby solutes accumulate in the (LIS) below the tight junction, raising the osmolality. Increased osmolality would then cause water to be drawn out of the surrounding cells and into the LIS, increasing the pressure inside the LIS and forcing the fluid out the basal opening. However, in recent years this model has been questioned based on a variety of factors ranging from the relative leakiness of the tight junctions, to inaccuracies of the values for water permeabilities predicted by the standing gradient model. A newer model suggests that the pathway is both paracellular and transcellular and driven by solute fluxes (Figure 1.3B). The fluid transport model becomes more complicated for airway epithelial cells that have thick 10 μm airway surface liquid which alters both solute and water uptake into the epithelia (**48**).

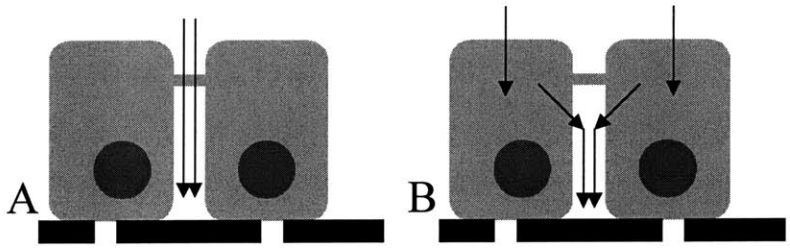

Figure 1.3: A) Paracellular fluid pathway, b) Transcellular and then paracellular fluid pathway.

1.2.2.4 Transcellular Pressure

Tarbell et al (54), investigated the role of a pressure difference across an endothelial cell layer on cell function. While the fluid flow in epithelial cells likely involves a large

transcellular component, in endothelial cells fluid follows a paracellular route. Step pressures ranging from 10 to 30 cmH_20 caused an increase in hydraulic conductivity of the cell layer and it was suggested that the increase in conductivity is due to increased shear stress in the endothelial cleft. The fluid shear stress was estimated to range from 25 dyn/cm^2 to 50 dyn/cm^2 depending on whether an open slit model or a fiber matrix slit model was considered. The cleft surface area was estimated to be ~18% of the luminal surface area for a cleft depth of 1μm.

The shear stress due to a pressure difference of 30 cmH_20 used in this study can be estimated from the following relationship, where ΔP is the pressure difference, h is the width of the intercellular space (assumed constant for this calculation), and L is the length of the space.

$$\tau_X=(\Delta Ph)/(2L) = 10 \text{ dyne/cm}2$$

10 $dyne/cm^2$ is on the order of magnitude shown to stimulate a biological response in endothelial cells exposed to a fluid shear stress along their apical surface (9).

A decrease in karatin production and a widening of intercellular spaces in glomerular visceral epithelial cells was seen in response to 100 Pa pressure applied to the basolateral membrane (6).

1.2.2.5 Hydrostatic Pressure

Hydrostatic pressure has been shown to elicit biological changes in epithelial cells. High hydrostatic pressures, on the order of 290-400 atm caused changes in epithelial cell morphology and in the components of the cytoskeleton (3). However, hydrostatic pressure had little effect on the volume flux across a layer of endothelial cells (54).

1.2.2.6 Deformation into the Porous Substrate

Localized deformations into the porous substrates on which many cell layers are grown has not been the subject of many studies. Tarbell et al. recognized that deformation into the porous substrate may occur in pressurized endothelial cell cultures,

but ruled it out as being insignificant in magnitude (54). Whether or not cells grow into the porous substrate, or deform into the pores in response to increased pressure is unclear. Filippatos et al. (13) showed that if the pores are large enough the cells grow into them.

1.3 Methods Used in this Study

The initial scope of this study was to develop a finite element model of an airway epithelial cell based on cell culture tests to determine the magnitudes and locations of increased stresses that would arise from a variety of stimuli. Previous tests performed with this cell culture system ruled out some mechanical stimuli such as substrate strain and hydrostatic pressure.

In the *in vitro* system used in this study, the epithelial cells are grown on a porous polyester substrate, which can deform slightly under pressure. Ressler, et al (37) measured the membrane strain due to transcellular pressures ranging from 5 to 20 cmH_2O by using digital images of the culture system under pressure. The maximum substrate deflection was measured and used to determine the average membrane strain. Under 20 cmH_20, the average membrane strain was 2.3%. Ressler then inserted a wire mesh beneath the cell layer and reduced the membrane strain to 0.2%. Reduction in the amount of membrane strain caused no significant change in the upregulation of Egr-1 mRNA, indicating that substrate strain does not play a significant role in the mechanotransduction process. However, it must be noted that in buckled airways the amount of strain the epithelial cells experience may be significantly greater. Ressler also showed that hydrostatic pressure in the range experienced by airway epithelia *in vivo* does not cause a significant upregulation in Egr-1 or in TGF-β.

While a couple potential mechanical stimuli in this *in vitro* system were ruled out, a number of stimuli still could be significant. As part of this study, cell-culture tests were performed to investigate activation pathways upstream from Egr-1 and to determine if osmotic shock is a significant stimuli. We used finite-element modeling to determine if the magnitude of deformation and if increased stresses due to a pressure difference were insignificant, or if they could potentially contributed to the biological response.

Finite element modeling has been used to model cells undergoing a variety of changes. In the fluid mechanics laboratory at MIT, current work is in progress to model a

neutrophil passing through a constriction. While epithelial cells do not behave with the properties of one single material, studies have been performed to characterize its mechanical response. Finite element modeling is useful to determine the magnitudes of stresses that a cell may experience and what sort of conformational changes the cell may undergo.

In addition, powerful imaging techniques have become available in recent years and provide invaluable information as to the morphology of the cells. In particular, the resolution and depth of field of transmission electron microscopy makes it ideal for determining the dimensions and morphology of a cell layer. Two-photon microscopy has the advantage that the cells can be imaged when they are alive and, in this case, immediately before and during pressure application.

1.4 Goals of Thesis

The primary goal of this thesis is to obtain a better idea of the magnitude and distribution of stresses associated with magnetic cytometry, deformation into the porous substrate, shear stress in the LIS, and pressure application. Stress and strain locations and magnitudes could be used to suggest which of the mechanisms would be likely to elicit a biological response and where the initiating event are likely to occur. Originally, shear stress and pore deformation were the primary mechanisms under investigation. However, our ability to examine issues relating to the flow in the intercellular gap was constrained due to a lack of knowledge regarding LIS dimensions and flows. This led to imaging studies based on the work of Spring and others. The goal of imaging was to determine if the intercellular spaces collapsed due to pressure gradients in the intercellular spaces, or if other phenomena occurred. Ultimately, this thesis aims to shed light on mechanisms that could contribute to mechanostimulatory events, and suggest pathways to study in more detail.

1.5 Thesis Outline

This thesis is broken into three main chapters providing a detailed exploration of epithelial mechanotransduction using three complementary techniques. Chapter two details the cell culture system used and discusses experiments performed, which show

that a transcellular pressure initiates a biological response. MAPK pathways are investigated to elucidate possible mechanical events contributing to the biological response. Osmotic shock tests were also performed in order to determine if the biological response of the cells to osmotic shock is similar to their response to a pressure difference. In chapter three, finite element models are presented to localize increased stresses and strains due to magnetic cytometry, pressure application, and fluid flow. Stress magnitudes were compared to find similarities between the models and to suggest thresholds for a biological response. Chapter four details imaging work performed both in this study and in others. In this study transmission electron microscopy and two-photon microscopy were performed and the results are presented in detail. Chapter five ties the cell culture, finite element, and imaging results together, summarizes the results, and ends with a look at future work. Together, modeling, testing, and imaging offer a unique insight into the complex response of epithelial cells to a transepithelial pressure, and help to increase our understanding of mechanotransduction and the pathological basis of asthma.

Chapter 2
Cellular Response to Mechanical Stimuli

In order to determine mechanosensory pathways it is important to first demonstrate that a specific mechanical stimulus elicits a biological response. Furthermore, information about biological pathways of upregulation, time courses, and locations in the cell where biological signal may be initiated, can indicate where and how mechanotransduction events occur.

Dr. Barbara Ressler, Dr. Melody Swartz, and Dr. Dan Tschumperlin performed most of the previous work investigating the biological response of pressurized airway epithelial cells. They worked out the methods for the cell culture system and the pressure apparatus used in this study and showed evidence that a transcellular pressure difference upregulates the genes associated with certain proteins that have been linked to airway wall remodeling. As part of this study, a few modifications on the original system were made, and the system was used to look at biologic evidence upstream of Egr-1 in order to isolate activation pathways. We also looked at the MAP kinases activated by an osmotic shock more closely, given that osmotic shock is known to cause biological changes in epithelial cells. Although the work presented in this chapter was conducted by a number of individuals, it is included here since it is important to illustrate the end point in my research; the biological response and the role of mechanotransduction in airway wall remodeling.

This chapter details the cell culture system and the pressure apparatus developed by Ressler and Tschumperlin. It provides a review of some mechanically responsive proteins and their link to asthma, and then discusses the results from MAP kinase and osmotic shock tests. The culture system described here was the same one used for the imaging tests, but with a few modifications that will be described in chapter 4.

2.1 Upregulation of Gene Expression and Protein Synthesis

Cell function is regulated by signals originating both inside and outside the cell. The binding to and activation of membrane spanning proteins can lead to the transcription of certain genes and changes in protein synthesis. The tyrosine-kinase signaling cascade is

one of the ways signals from the outside environment lead to gene transcription in the nucleus. Mechanical forces and activation of membrane spanning proteins leads to a signaling cascade that culminates in the phosphorylation of mitogen activated protein (MAP) kinases. These MAP kinases go directly to the nucleus where they lead to gene transcription that in turn promotes cell growth and leads to the release of a variety of proteins that can alter the environment around them (29). Egr-1, TGF-β and endothelin-1 (ET-1), are just a few of the genes upregulated by MAP kinases that are implicated in airway wall remodeling.

In order to predict what protein kinase and genes are upregulated and transcribed in airway epithelial cells a variety of step are necessary. First, a cell culture system was developed that replicates the *in vivo* epithelium. Next, the *in vivo* forces were mimicked, and finally, tests were performed to indicate what protein kinases and transcription factors are activated in response to the applied forces.

2.2 Methods

2.2.1 Cell Culture

Passage 2 normal human bronchial epithelial cells (NHBE, Clonetics-BioWhittaker, San Diego, CA) were seeded on tissue culture treated plastic at 37°C and 5% CO_2, and suspended in Bronchial Epithelial Growth Media (BEGM, Clonetics) supplemented with bovine serum albumin (1.5μg/ml), and retinoic acid (50 nM). The cells were transferred to uncoated nucleopore polyester Transwell Clear tissue inserts, 12- and 24- mm in diameter (0.4 μm pores, Corning Costar, Cambridge, MA). Approximately 50,000 cell/well for the 12-mm inserts and 100,000 cells/well for the 24-mm inserts were plated on each insert. Once plated, the cells were fed a 1:1 mixture of Dulbecco's Modified Eagle's Medium (DMEM, Life Technologies, Frederick, MD) and BEGM apically and basally every other day. Meanwhile, the cells were kept in an incubator at 37°C with 5% CO_2 and 95% air. When the cells reached confluence the media on the apical surface was removed in order to make air-liquid interfaces. Without media on the apical surface, the cells differentiated into a pseudostratified layer similar to that seen *in vivo* (Figure 2.1). The differentiated cells secreted mucus and displayed

prominent cilia. The media on the basal surface of the cells was changed every other day until the cells were fully differentiated and confluent.

For the studies characterizing gene expression, the media was changed to minimal "IT" media, consisting of a 1:1 mixture of bronchial epithelial basal media and DMEM with insulin (5.7μg/ml), penicillin (100units/ml), streptoycin (100μg/ml), and transferrin (5μg/ml), approximately 16 hours prior to use. For the imaging studies, full media was used for the full duration of the experiments.

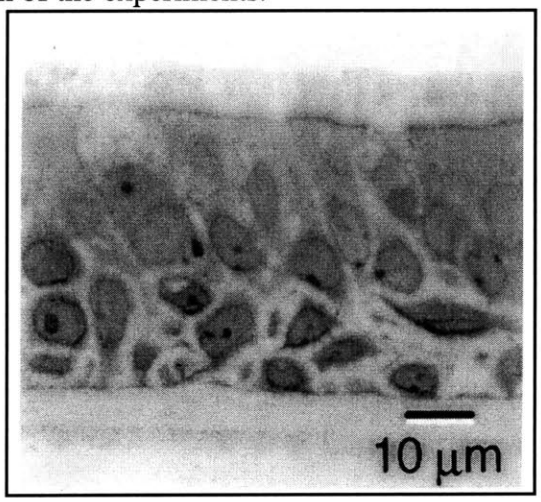

Figure 2.1: Pseudostratified differentiated layer of airway epithelial cells (Matsui).

2.2.2 Osmotic Shock

The osmotic stress consisted of IT media supplemented with NaCl. The NaCl solution was made the day before was placed in an incubator overnight to let the temperature and pH equilibrate. To shock the cells, 250μl of NaCl was added to the 2.25 ml of basal media. Isotonic media was added to a subset of wells to use as a control.

2.2.3 MAP Kinase Phosphorylation

MAPK phosphorylation was detected using commercial kits that include antibodies for each MAPK and the phosphorylated form of each protein (Cell Signaling Technology, Beverly, MA). After stimulating the cells they were lysed in SDS sample buffer consisting of 62.5 mM Tris-HCl, 2% w/v SDS, 10% glycerol, 50 mM dithiothreitol, and 0.1% w/v bromphenol blue. The lysates were collected in a sample buffer and immunoblotting techniques were performed.

2.3 Pressure Apparatus

The pressure apparatus described previously (37) was used for all pressure experiments (Figure 2.2). Briefly, a rubber stopper is press fit into the top of the Transwell filter and an airtight seal is formed. A pressure tank with 5% CO_2 95% air is connected to a three-way valve directing the air to a manometer and to the cells via a drilled hole in the rubber stopper. The compressed air fed into the top of the rubber stopper pressurizes the apical surface of the cells. Since the cells are grown on a porous filter, the basal surfaces of the cells are at atmospheric pressure, neglecting any pressure drop that might arise due to fluid transport. The monometer is used to measure the pressure of the compressed air relative to atmosphere and the pressure is allowed to stabilize before directing the compressed air to the apical surface of the cell layer.

2.4 Early Growth Response-1

Egr-1 is an immediate early gene and primary response transcription factor shown to activate PDGF (24), which leads to increased collagen production (36), a characteristic of airway wall remodeling in asthmatics. Egr-1 is upregulated due to a variety of mechanical stimuli including fluid flow (33), shear stress (44), and osmotic stress (7). Its role in airway remodeling and its early response to mechanical stress make it an ideal gene to study.

As discussed earlier, Ressler, in her experiments with pressurized epithelial cells showed that Egr-1 mRNA is upregulated in a time and pressure dependent manner. A response was seen after 1 hour, but diminished by 6 hours. Then the cells were pressurized for one hour at 0, 2, 5, 10, and 20 cmH_2O. At 0 and 2 cmH_20 no increase in Egr-1 RNA was detected and it was concluded that those pressures are below the threshold value for eliciting a response (37).

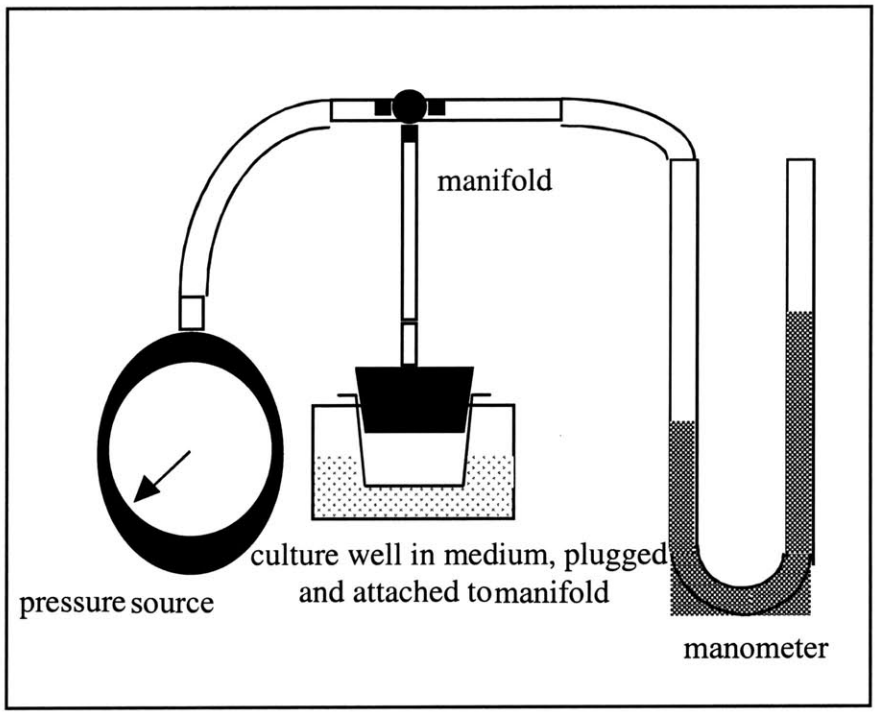

(A)

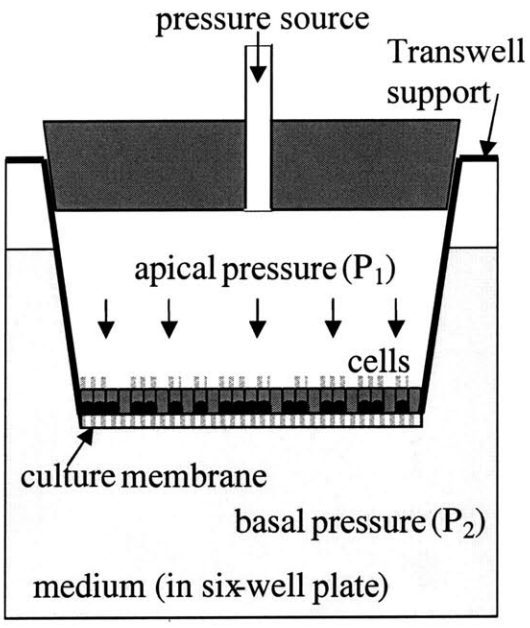

(B)

Figure 2.2: A) Schematic of the pressure apparatus showing the Transwell support connected to both a pressure source and a monometer. B) Schematic of one Transwell support with a transcellular pressure difference.

2.5 Mitogen Activated Protein Kinase Results

Egr-1 is regulated by a family of MAP kinases. MAP kinases are important because they are activated by a diverse set of factors, including mechanical forces. In addition, they are powerful enzymes that regulate a number of transcpription factors in the nucleus, which control basic cell function ranging from differentiation, to apoptosis, to growth. Extracellular signal related kinase (ERK), c-Jun NH2-terminal kinase (JNK), and p38 are three members of the MAP kinase family. ERK is upregulated due to shear-stress (44, 53), hypertonic stress (20), strain (38, 63) and altered adhesion (53). Hypertonic stress has also been shown to activate p38 and JNK and mechanical strain to activate JNK, ERK, and p38 (38). In endothelial cells, shear stress and strain activated JNK, ERK, and p38, although shear stress increased ERK and p38 more than strain did, suggesting different types of mechanoreceptors in endothelial cells for shear stress and strain. Determining what mechanically responsive MAP kinases family members are upregulated due to a pressure difference can provide more information about what mechanotransduction pathways are at work in pressurized airway epithelial cells.

Using the pressure apparatus described previously, cells grown in 24-mm culture wells were pressurized with 30 cmH_2O for varying amounts of time. Immediately following pressure application the cells were lysed and an immunoblot was performed using antibodies for each MAPK and antibodies specific for the phosphorylated, or active, form of each MAPK. In Figure 2.3A the top row of blots shows the amount of non-phosphorylated ERK in each sample, demonstrating equal loading of protein in each lane. The lower blots show the amount of activated MAP kinases. The results indicate that the ERK pathway was upregulated in a time dependent manner while the JNK and p38 pathways were not.

2.6 Osmotic Shock Results

The cell membrane is semi-permeable and is much more permeable to water molecules than to ions. A pressure difference that forces water to move across the cell membrane can be equated to an osmotic shock that drives fluid across a ionic concentration gradient. *In vivo*, cells exist in an isotonic environment controlled by

sodium, chloride, calcium, phosphate, and potassium ion channels. An osmotic challenge disrupts the ionic homeostasis by altering the concentration of ions in the extracellular matrix. The cell compensates with a volume change, moving water ions to counter balance the osmotic stress. When the osmotic challenge is a solution with a high concentration of solutes, water leaves the cell, and when the solution is low in solute, water enters the cell causing it to swell and even rupture. Since an osmotic stress can act by itself to regulate MAP kinases (20) and Egr-1 (7) in canine kidney cells, it is possible that an osmotic change caused by the pressure difference in our apparatus could account for the upregulation of Egr-1 and the activation of ERK. Cell culture tests were performed to determine if hypertonic shock is a mechanosensory pathway in pressurized airway epithelial cells. An osmotic concentration equivalent to the imposed pressure difference of 30 cmH_2O was determined from the following relationship:

$$\Delta P = RT\Delta C$$

$$\Delta C = 1.15 \text{ mOsm/L}$$

ΔP is the pressure difference, R is the ideal gas constant, T is the temperature, and ΔC is the change in osmotic concentration. An osmotic shock of 1.15 mOsm/L NaCl and of 200X the equivalent value, or 230 mOsm/ml NaCl, was applied to the basal surface of the cells and the results were compared to those from the pressure studies. Immunofluorescence was performed on each sample to determine which MAP kinases were activated. The results are shown in Figures 2.3B and 2.4. An osmotic shock of 1.15 mOsm/ml did not significantly increase the phosphorylated form of ERK. Even the 200X concentration did not increase the phosphorylated form of ERK as much as the 30 cmH_2O pressure difference did. Figure 2.3B indicates that a hypertonic stress of 230 mOsm/L activated p38, JNK, and ERK. Comparing the results to those for the pressure stimulus shows that different MAP kinases are activated in response to pressure and to osmotic shock.

It is unclear how an osmotic shock leads to a biological response. Niisato, et al. (32), suggest that in osmotically shocked cells it is the membrane stretch caused by

volume change and not the osmotic difference across the cell membrane that induces an upregulation of specific MAP kinases.

2.7 Implications of Results

These results indicate that a transcellular pressure causes an upregulation of Egr-1 by activating the MAP kinase ERK. The pathway of upregulation is different than for osmotic shock, suggesting that other mechanisms or a combination of mechanisms are at work to elicit a biological response. The osmotic results appear to suggest that when the cells are pressurized there is no significant osmotic related volume change. However, limitation in the osmotic test methods and imaging experiments cause the results to be somewhat inconclusive. When the NaCl was introduced to the cell layer in this study it was applied beneath the culture well that the cells are gown on. The pores in the substrate may significantly limit the diffusion of the NaCl into the cell layer, and reduce the concentration that reaches the cells. In addition, it has been shown that applying an osmotic shock to the basal surface of a cell layer produces different results from osmoticaly shocking the apical surface. Shocking the basal surface with 150 mM raffinose caused the basal cells to shrink in volume, while shocking the apical surface caused the larger apical cells to shrink (30). Imaging experiments in Chapter 4 showed that a volume change does occur, although whether or not the basal or apical cells changed volume was unclear. The important results of the osmotic shock experiments was that different pathways are activated for a transcellular pressure and an osmotic shock. Separate pathways indicate that while an osmotic induced volume change may occur in the pressurized cells it is probably not the primary mechanosensory mechanism.

The biological responses discussed in this chapter provide the groundwork for the rest of this thesis. The fact that Egr-1 is upregulated and ERK is activated provides further evidence that the application of a compressive force, similar to that seen in asthmatic airways, stimulates a biological response that has the potential to contribute to airway wall remodeling. The remainder of this thesis investigates the connection between force application and the biological response.

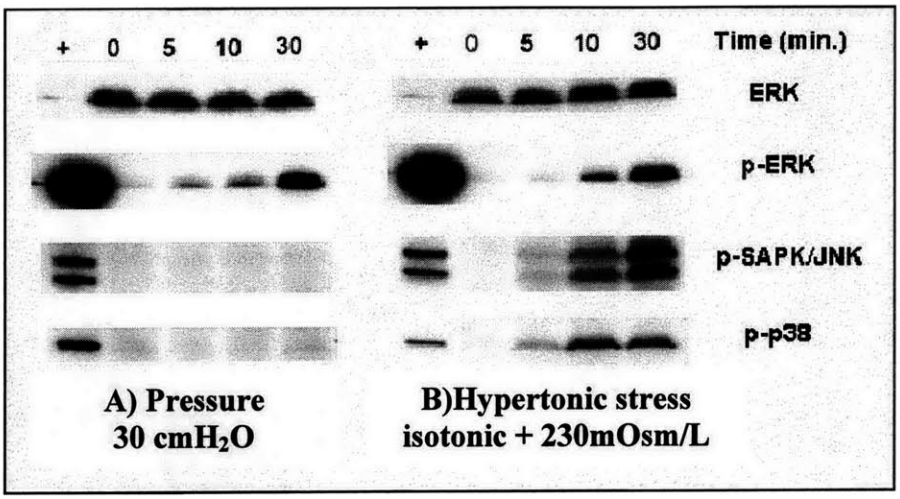

Figure 2.3: Immunoblots. A) A transepithelial pressure of 30 cmH_2O increases p-ERK in a time dependant manner. In B) hypersomotic stress increases p-ERK, p-SAPK/JNK, and p-p38 in a time dependent manner.

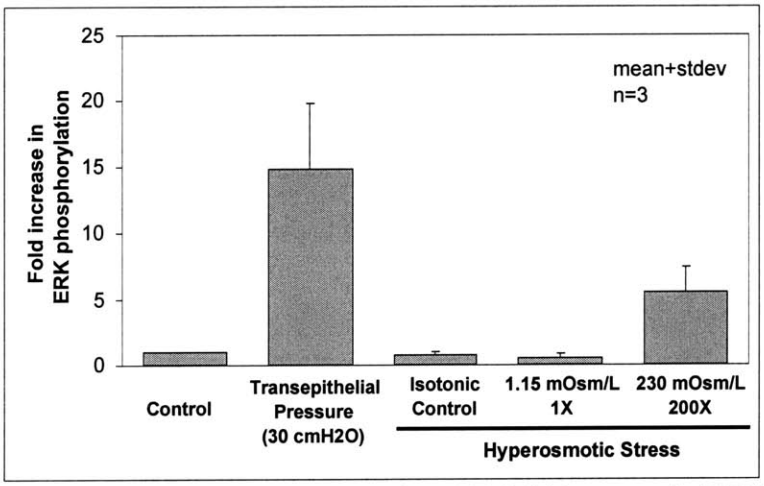

Figure 2.4: 30 cm H_2O caused a 14% fold increase in ERK phosphorylation while an equivalent osmotic shock of 1.15 mOm/L did not increase ERK phosphorylation above control levels. 230 mOsm/L increased ERK phosphorylation, but not as significantly as the pressure application.

Chapter 3
Finite Element Models

Based on the upregulation of Egr-1 and activation of ERK in response to a transcellular pressure difference, it is apparent that mechanotransduction occurs in airway epithelial cells exposed to a transcellular pressure difference. However, the link between the pressure application and the biological response is still unknown. Finite element models have proven useful in many applications to obtain insight into locations of increased stress and strain and to determine where conformational changes occur. For this reason, a finite element model of a bronchial airway epithelial cell was developed to uncover areas where increased stresses and strains could potentially contribute to, or cause, a biological response.

The first finite element model was constructed to determine the location and magnitude of stresses due to magnetic cytometry. The second two models pertain to events in pressurized epithelial cells. One model consisted of a single epithelial cell deforming into a porous substrate, and other consisted of two cells separated by a narrow intercellular space through which flow can occur.

The goals of the finite element models were 1) to determine the magnitude and location of any large stresses that occur, 2) to compare the stresses and strains for each of the models to determine if there may be a threshold value that elicits a response, and 3) to determine the effects of pressure on the LIS and if shear stress in the LIS could be a potential mechanism.

3.1 Bronchial epithelial cell model

A single epithelial cell was modeled based on the geometry obtained from TEM images. The airway epithelial cell is columnar and consists of a cytoskeleton surrounding a nucleus. In the model the cytoskeleton has height, h and width, w. The nucleus was modeled as a circle with radius r. The cytoskeleton and nucleus are surrounded by a thin lipid bilayer acting as a barrier to the outside environment and as a support, providing resistance to structural changes inside the cell. The lipid bilayer is modeled as a thin membrane with thickness, t (Figure 3.1).

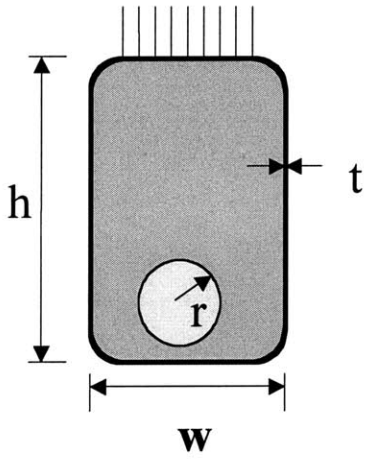

Figure 3.1: Basic cell model. The cell consists of a nucleus and cytoskeleton surrounded by a thin membrane. Cilia are present on the apical surface.

3.2 Finite element analysis: Definition

In a finite element analysis a mathematical model idealizes a physical structure and the response of the model is determined by differential an/or integral equations. The physical model is represented by beam and truss elements that are connected at nodes. In the displacement-based finite element method the displacements of the nodes that result in the final state of equilibrium is determined as well as the force balance equations at the nodes that cause the nodal displacements. When the final displacements of the nodes are calculated the internal stress distribution is calculated. The stress distributions must then be interpreted in the context of the idealized structure (2).

In the analysis an element stiffness matrix, K, is determined from material properties and geometry, and used to balance the reaction forces of the structure, KU, with the applied external forces acting on the structure, R. The characteristic equation is thus R=KU, which is analogous to a spring where and external force, F, is balanced by the displacement of a spring with constant k that represents the geometric and material properties of the spring, F=kx. Displacement based finite-element modeling solves for the displacement vector U and from the displacements the stresses in the internal elements can be determined from the mathematical model. These results are predicted values for the actual structure in question and are only as accurate as the mathematical model.

The finite element program ADINA (Watertown, MA) was used for all models. The Theory and Modeling Guide provides an extensive reference for the capabilities of ADINA (1).

3.3 Finite element model: Methods

In finite element analyses, 2D plane strain or plane stress elements are usually treated as isoparametric displacement-based finite elements. However, when the material used is incompressible with $\nu \sim 0.50$ the elements are treated as mixed interpolation elements, which means that displacement (u) and pressure (p) variables are interpreted separately. Mixed u/p interpolation is used for nearly incompressible materials because the pressures variables are hard to determine and can be statically compressed out.

For the mixed interpolation method the 9/3 element, with 9-node displacement variables and three pressure variables is preferred. 4-node elements with one pressure degree of freedom and the option to add more displacement degrees of freedom is another option, but should not be used when bending effects are significant. 9-node elements take more time computationally, but provide more accurate results. In this analysis 9-node elements are used to model both the cytoskeleton and the nucleus in the epithelial cell analysis.

ADINA uses local displacement degrees of freedom in the analysis. In the 2D analysis three degrees of freedom, Y,Z-translation and X-rotation are specified. For the nonlinear analysis the Total Lagrangian (TL) formulation is used to linearize the equilibrium equations. The TL formulation uses an incremental Lagrangian analysis approach and all static and kinematic variables are referred to the original configuration at time 0 (Bathe text).

3.3.1 Integration method

For all calculations, numerical 3x3 Gauss integration is used. ADINA automatically chooses the default Gauss integration orders for rectangular 9-node elements. During a nonlinear analysis when the large displacement formulation is used, the integration points along the elements shift spatial positions. However, the same material particles will still

correspond to the same integration points. After the displacement and pressure variables are determined, the stresses are calculated from the strains.

3.4 Finite element model: 2-D plane strain elements

TEM images show that airway epithelial cells have a three dimensional cubical geometry. However, since the cells do not vary significantly in cross-section, and the forces act in-plane, two dimensional elements with a unit thickness were chosen to represent the cytoskeleton, nucleus, and membrane.

For this analysis, 2D elements are defined in the Y-Z plane. Due to force application in the Y- and Z- directions and the lateral confinement of the cells, the strains will predominately be in the Y- and Z- directions, (ε_{yy}, ε_{zz}) with a small shear strain contribution. Since the strain in the X-direction (ε_{xx})and the shear strains γ_{xy} and γ_{xz} will be negligible, 2-D plane strain elements were selected. Figure 3.2 depicts a 2-D plane strain element.

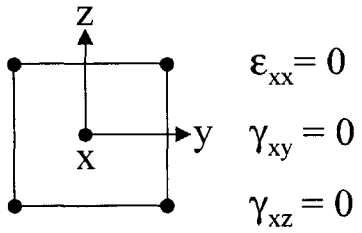

Figure 3.2: Plane strain element

3.5 Finite-Element Model: Isoparametric beam elements

Nonlinear plane strain isoparametric beam elements were chosen to model the cell membrane. For the iso-beam elements, large displacements were selected and small strains are automatically assumed by ADINA. The advantage of iso-beams, verses standard 2-node Hermatian beams, is that they accurately model the geometry corresponding to large displacements.

Iso-beams are defined by the rst coordinate system as depicted in Figure 3.3. While 3-node iso-beams can be curved in three-dimensional space they must initially be defined in the r-s plane. The X-rotation degree of freedom was not fixed to allow the beams to rotate

and curve. 2-D element numerical integration is performed in the r-s plane. For the computation, isoparametric interpolation is used with Gauss numerical integration. The default integration order is 2-point integration in the r- direction for 3-node iso-beam elements. The iso-beam elements can only be used with constant rectangular cross-sectional areas.

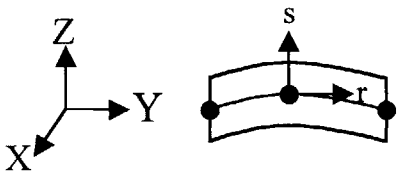

Figure 3.3: A 3-node 2-D iso-beam element. The t-direction is into the page.

3.6 Finite element model: Assumptions

3.6.1 Continuum model

In vivo the cytoskeleton of epithelial cells consists of a network of microfilaments, microtubules, and intermediate filaments. Over short time scales, the cytoskeleton behaves more like a viscoelastic material than a linear elastic material, due the mechanical properties of each of the components (23). However, for a static analysis over a long time scale and on a length scale large compared to the spacing between the filaments, the cytoskeleton can be modeled as an elastic continuum. Continuum models have limitations since they neglect the interactions of the individual filaments that comprise the cytoskeleton, but for a general localization of areas of increased stress, continuum models are quite appropriate, relatively easy to solve, and still provide useful insight.

3.6.2 Large displacement/small strain formulation

A large displacement formulation was chosen to account for nonlinearities in the model. In ADINA large strains are not allowed with a linearly elastic isotropic material. Instead, ADINA uses an intermediate kinematic formulation that accounts for large displacements and rotations, but not for large strains. With a small strain formulation, inaccuracies may occur when strains are in excess of 5%.

For a large displacement formulation, ADINA uses engineering (normal) stresses and strains as inputs and Cauchy (true) stresses and Green-Lagrange strains as outputs. For the small strain formulation, the Green-Lagrange strains are equivalent to engineering strains without rigid body rotations. The small strain assumption requires that the area of the elements is constant throughout the integration. The strain magnitudes are not large enough to significantly increase or decrease in the area of any deformed element.

$$\text{Engineering strain: } e_o = \frac{l - l_o}{l_o}$$

$$\text{Green-Lagrange strain: } \varepsilon = \frac{1}{2}\frac{l^2 - l_o^2}{l_o}$$

$$\text{The relationship between the true stress } \tau \text{ and the engineering stress } \sigma\text{: } \tau = \frac{\sigma S_o}{S}$$

$$\text{For incompressible materials: } \tau = \frac{\sigma L}{L_o}$$

3.6.3 Incompressible isotropic linear elastic material

Cells are complex biological systems and cannot be characterized by one material model. Cells consist of a large amount of water, rendering them nearly incompressible, but the membrane is porous allowing for some water loss when compressed. A Poisson's ratio of 0.49 accounts for the nearly incompressible nature of the cells.

Due to the distributed network of the cytoskeleton and the dense DNA and lamin fibers of the nucleus, both can be assumed to be isotropic and homogenous. It has been shown that cell layers exposed to a shear stress develop stress fibers in the direction of the flow. However, pseudostratified epithelial cells are not known to have a preferential direction of alignment or areas of inhomogenaity.

A variety of mechanical manipulation techniques, such as micropipette aspiration and cell poking, have demonstrated that endothelial cells have an elastic material response due to the cytoskeleton network (51). Aspirated leukocytes initially display an elastic response, which is followed by a viscoelastic response that eventually reaches a final steady-state response after tens of minutes (46). Linear models are used extensively to model the behavior of cell types, including cultured endothelial cells (41), and in red

blood cell aspiration only small nonlinearities were seen over time (11). These studies show that while the mechanical properties of cells are complex, for a steady state analysis over a long time scale, a linearly elastic material is a reasonable choice.

3.7 Output parameters

A number of stresses, strains, displacements and forces are determined by a finite element analysis. Effective stress is one of the more useful stress invariants for this analysis since it subtracts out the contribution due to the isotropic compression, which in this case is a large applied pressure. Effective stress is defined as:

$$\sigma = \sqrt{\frac{1}{2}\left(\left(\tau_{xx}-\tau_{yy}\right)^2+\left(\tau_{xx}-\tau_{zz}\right)^2+\left(\tau_{yy}-\tau_{zz}\right)^2+6\left(\tau_{xy}^2+\tau_{xz}^2+\tau_{yz}^2\right)\right)}$$

The pressure component of the stress is also useful and it is defined as:

$$p = -\frac{\tau_{xx}+\tau_{yy}+\tau_{zz}}{3}$$

Other variables used to interpret the results the following sections are Y- and Z-displacement, stress-YY, stress-ZZ, strain-YY and strain-ZZ for the cytoskeleton, and stress-rr, stress-tt, strain-rr, and strain-ss for the membrane (Figure 3.3).

3.8 Cell Model

3.8.1 Geometry

The basic cell dimensions were obtained from TEM images. In the model, the cells were specified as 20 μm tall and 15 μm wide with a unit thickness. The nucleus is circular with a radius of 3μm and the membrane is 6 nm thick.

3.8.2 Materials

The cytoskeleton is modeled as a linear elastic isotropic material with a Young's Modulus of 100 Pa. Few studies have been performed to determine the stiffness of epithelial cells and the results vary depending on the test performed. Using a micropipette technique Theret et al. (55) determined the effective Young's Modulus of attached endothelial cells to be on the order of 80 to 130 Pa. Sheared cells had a higher stiffness

ranging from 200 to 800 Pa. Based on Theret's results and others, we determined a Young's Modulus of 100 Pa to be within a reasonable range. The nucleus is three to four times stiffer than the cytoskeleton (Guilak,44). In this model the Young's modulus for the nucleus was specified as 1000 Pa. Parameters chosen for the cell membrane are based on the characteristics of a lipid bilayer. For a lipid bilayer, the areal elasticity is on the order of 0.57 J/m^2 (Needham) while the bending stiffness is approximately $4x10^{-20}J$ (Hwang, 44). An equivalent Young's Modulus of 10^7 Pa is consistent with both the areal and bending stiffness. All materials were assumed to be incompressible. For the membrane, ν=0.49 and for the cytoskeleton and nucleus ν = 0.4999.

The inherent problems that arise with finite element modeling include accurately representing the physical model. Few studies have determined the stiffness of endothelial cells, and every test provides different results. The results used in this study are taken from literature and provide and a reasonable starting point. As part of this analysis, cytoskeleton and membrane stiffness values were varied by a factor of 10 to determine the dependence of the results on the material properties.

3.8.3 Elements

The cytoskeleton and nucleus are modeled with 9-node plane strain elements. Large displacements and small strains were specified, and a mixed interpolation, steady-state, analysis was performed. The membrane was modeled with 3-node iso-beam elements and was sufficiently thin and the curvature sufficiently small so the bending stiffness is negligible. The membrane iso-beam elements were used with a large displacement formulation. The membrane and the cytoskeleton and are attached through shared nodes.

3.9 Bead Model

In magnetic cytometry, magnetic beads are rigidly attached to a monolayer of cells through integrins in the cell membrane. A finite element model was developed to determine the magnitude and location of increases stresses and strain in response to magnet bead twisting. The finite element bead model consisted of a single 0.4 um bead attached to a monolayer of three cells (Figure 3.4). The Young's modulus and Poisson's

ratio of the bead was specified as 10,000 Pa and 0.30, respectively. The three cells are rigidly attached to each other so that they move as one body. The lateral walls of all the cell were not constrained in order to see the effects of rotating the bead on the neighboring cells. The lateral walls could move freely in the Y-Z plane. The basal surface was constrained in the Z- but not in the Y-direction.

The bead is attached rigidly to the apical surface of the middle cell over 30 degrees of the cell. Rigid links, representing integrins, link the bead to the nodes shared by the membrane and the cytoskeleton beneath the bead. Thus, rotation of the bead is affected by both the bending stiffness and tension of the membrane, and by the stiffness of the

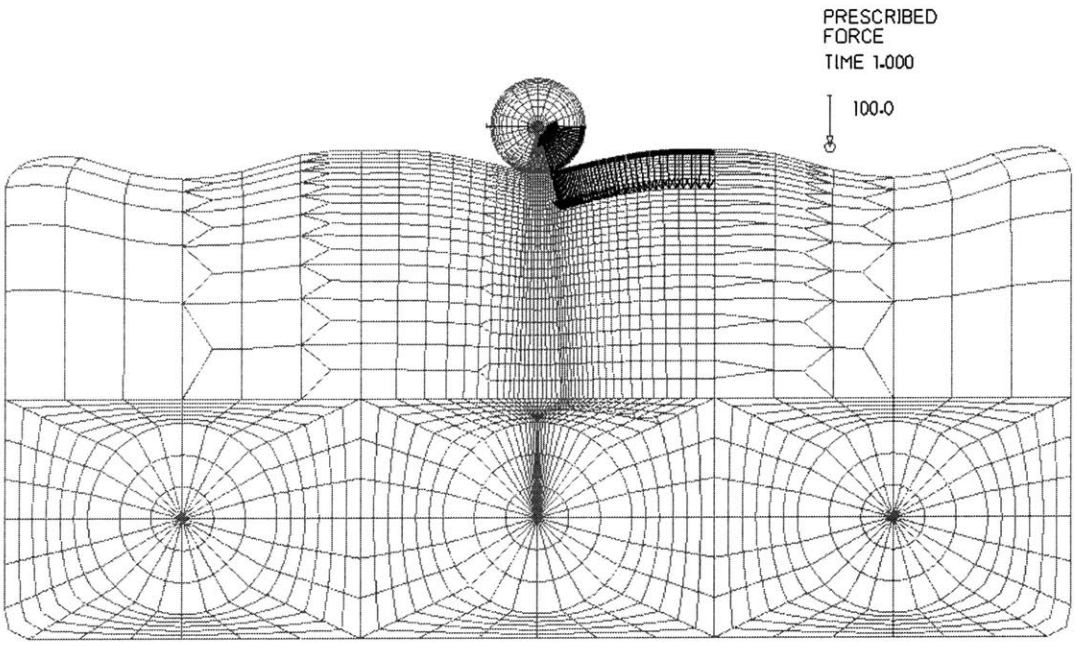

Figure 3.4: Bead mesh. Three cells are connected and the circles in the lower half of each cell represent the nuclei. The bead is rigidly attached to the center cell over 30 degrees and the contact surface is in black.

cytoskeleton. Similarly, *in vitro* beads are attached to the cytoskeleton by integrins that span the membrane. However, since the membrane is fluid the integrins move through the membrane and the tension in the membrane has little effect on the movement of the bead. To determine the effects of the membrane, the bead finite element model was also

analyzed without a membrane, and then without the membrane attached to the cytoskeleton through shared nodes.

In the 2D model, the bead is represented as a cylinder of unit length in the x-direction. A 100 pN/μm force was applied to the center of the bead in the +y-direction. A contact surface was prescribed on the right side bead where it is not rigidly attached to the cell. The matching contact surface is on the cell membrane to the right of the bead. The contact surface prevents the nodes on the bead and the cells from overlapping.

3.9.1 Bead model: Results

A force of 100 pN/μm applied to the center of the bead caused the bead to rotate and move 2.68 μm in the +Y direction. Since the bead is rigidly attached to the cell and the membrane, both are pulled in tension to the left of the bead and compressed under and to the right of the bead. Figure 3.5 shows the effective stress field in the vicinity of the bead. The highest stress field is localized to the left of and under the bead. The maximum effective stressed on the left side of the bead are more than 100 kPa but falls off rapidly a few microns away. Stresses as high as 15 Pa are seen in the nuclei of the adjacent cells and up to 7 Pa at the basal membrane (Figure 3.6).

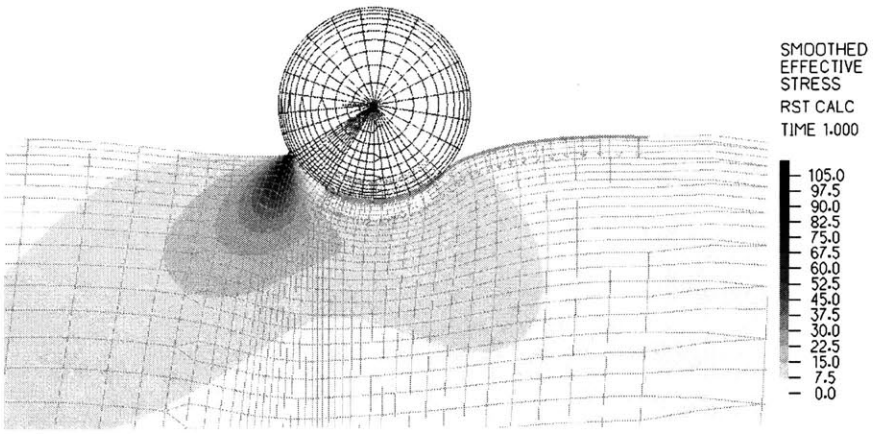

Figure 3.5: Bead Model: Effective Stress

The maximum strain-YY in the cytoskeleton approached -35% to the left of the bead and +20% below the bead (Figure 3.7). The maximum strain in the Z-direction reached 50%. High strains are localized in the vicinity of the bead and fall below 5%

approximately 2 μm from the bead. Figure 3.8 shows the pressure field near the bead. The pressure is a maximum of 30 Pa beneath the bead and falls to -100 Pa to the left of the bead. The maximum ZZ- and YY- stresses in the cytoskeleton were 410 and 147 Pa, respectively, and were located to the left of the bead.

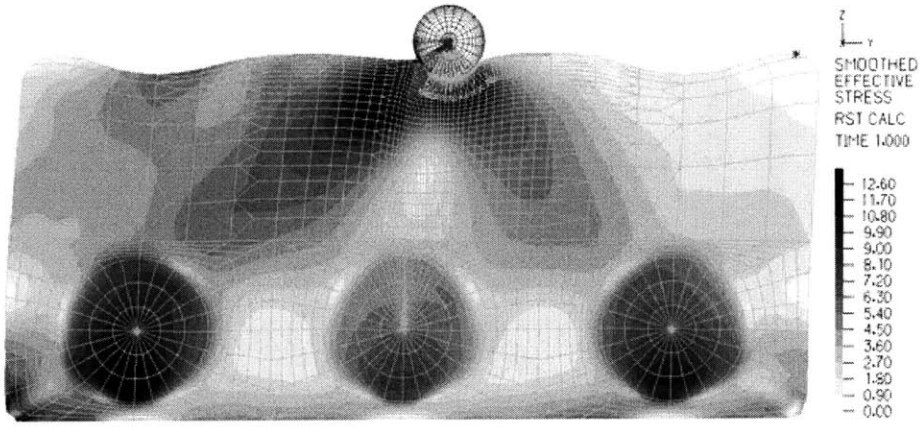

Figure 3.6: Plot of effective stress for whole model. Stresses over 10 Pa below the bead and in the nuclei of all three cells.

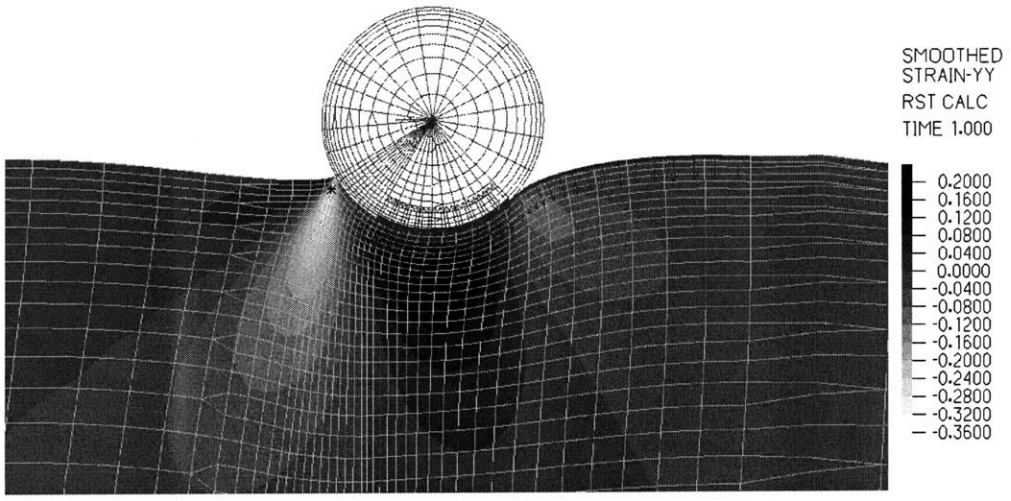

Figure 3.7: Bead model: strain-YY near the bead

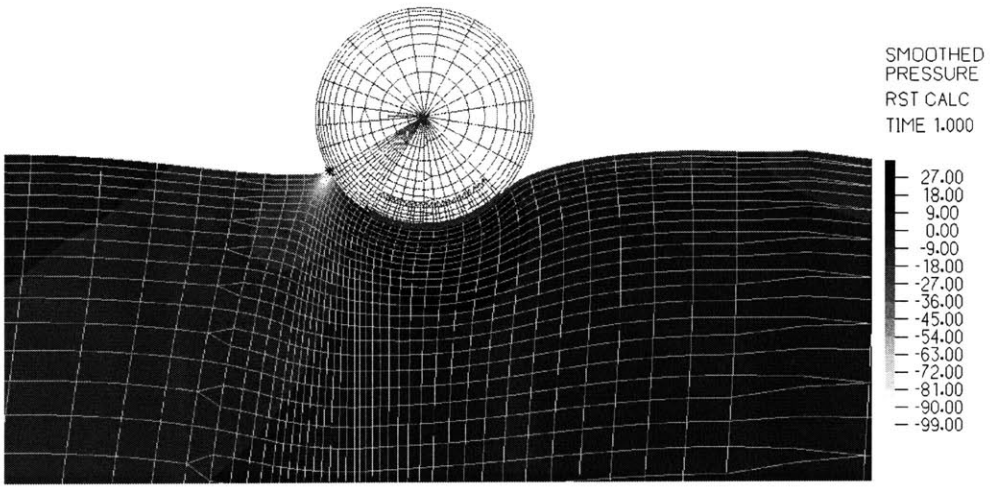

Figure 3.8. Bead Model: pressure near the bead

Figure 3.9 shows a graph of Y-displacement verses force graph for the node at the center of the bead. The graph shows that the relationship between the force and the displacement is not linear despite our assumption of constant elastic properties. The nonlinear response arises from the large displacement formulation and from inaccuracies stemming from the small strain assumption. Since the bead is rigidly attached to both the membrane and the cytoskeleton, the combined response of the cytoskeleton and the stiffer membrane determine the displacement of the bead. The membrane resists any large strains and it acts to inhibit the movement of the bead.

As the bead rotates it pulls on the cell membrane causing maximum stress of 28 kPa in the rr- direction. Effective stresses in the membrane are a maximum of 24 kPa and the maximum membrane strain is 0.25%, verifying that the small strain assumption for the membrane is accurate.

A finite element analysis was also performed for a cell without a membrane. Without the membrane acting to resist cytoskeletal deformation only 10 pN/μm applied to the center of the bead created strains of up to 68% and a maximum Y-displacement of 0.83 μm in the cytoskeleton. In another model, in which the bead was attached to the membrane, which was not attached to the cytoskeleton, the membrane separated from the cytoskeleton and the finite element analysis did not converge to a solution.

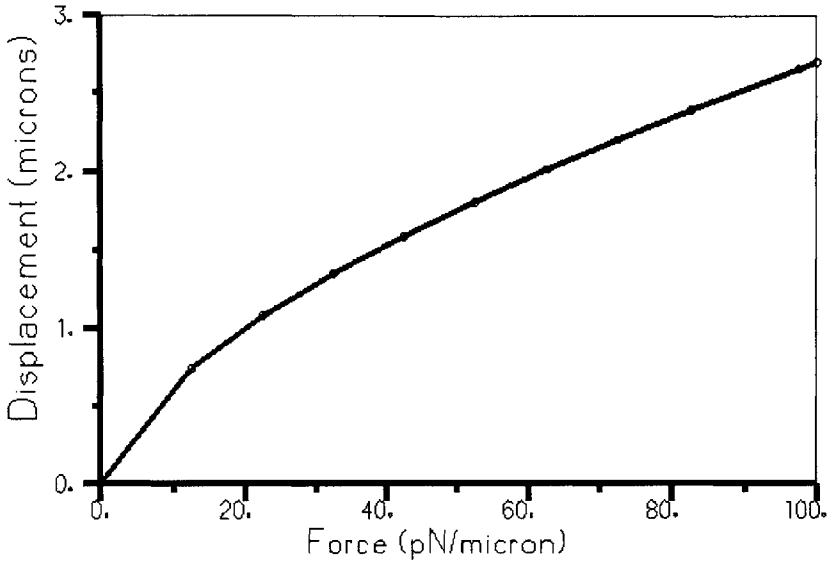

Figure 3.9: Plot of displacement verses force for the node at the center of the bead.

3.9.2 Bead model: Discussion

The finite element model shows that magnetic cytometry creates localized stress concentrations in the cell near the point of attachment to the bead. However, strain values in the cytoskeleton near the bead are significantly greater than 5%, indicating that a large strain analysis would be more appropriate. Compared to the initial assumptions and generalizations in the mathematic model, the error associated with the small strain assumption will be minimal for the model as a whole. Large displacements and strains in the membrane verify that a large displacement / small strain formulation is appropriate for the iso-beam elements.

The movement of the cell layer in the +Y direction contributes to the increased stresses in the nuclei. Since the nuclei are an order of magnitude stiffer than the cytoskeleton, they experience a great effective stress as they resist the movement of the cytoskeleton. Increased stresses near the bottom of the cells arise from cells pulling on the basal membranes, which is fixed to the substrate.

Finite element models without the membrane, and without the membrane attached to the cytoskeleton, portray the importance of the membrane. The models demonstrate the role of the membrane in resisting deformation and the importance of integrins that physically connect the ECM to the cytoskeleton.

The value of a bead twisting computational model is to localize the areas of increased stress and strain and to determine what magnitude of stresses could initiate the biological response. The bead model shows that increased stresses near the bead and in the nuclei could potentially play a role in mechanotransduction. Comparing the results for a bead twisting model to models with other types of force application can indicate threshold stress values for inducing biological changes in certain cell systems and can indicate if cells sense mechanical forces in the same way or if there are different pathways for mechanotransduction.

Exposing a layer of airway epithelial cells to a transmembrane pressure is an example of another type of force application. The following pressure model was analyzed to indicate locations of increased stresses in the *in vitro* model discussed in Chapter 2.

3.10 Pressure Model

A finite element model was developed to analyze the mechanical response of a single airway epithelial cell grown on a porous substrate to a transcellular pressure difference. The model consisted of a single bronchial epithelial cell model as described previously, attached to a substrate with a single 0.4 μm pore in the center (Figure 3.10). The radius of curvature of the sides of the pore was 0.1 μm. The lateral walls of the cell were free to move in the Z-direction, but were constrained in the Y-direction, on the assumption that the neighboring cells prevent the cell from bulging in the Y-direction. The basal surface of the cell was constrained in the Z-direction, except for in the 2 μm to either side of the pore. In the vicinity of the pore a contact surface was defined between the basal surface of the cell and the underlying substrate. The contact surface allows the membrane to move in the downward in the Z-direction into the pore, without penetrating the substrate. The basal membrane was allowed to move in the y-direction to pull into the pore. In culture, the cells attach to the underlying substrate through cell adhesion molecules. The contact surface in this model neglects adhesion in the vicinity of the pore in order to allow the membrane to move freely into the pore. Cell-substrate adhesion sites have little mechanical rigidity and when exposed to increased tension, detach by "cell peeling" (59). Therefore, it is reasonable to assume that if the applied force was large enough the

tension in the membrane would disrupt the cell adhesion molecules and allow the membrane to move towards and into the pore. The model also allows the membrane to pull around the basal sides of the cell.

Due to the limitations of 2D linear elastic elements under large pressures, instead of applying the pressure to the apical surface of the pore, the pressure was applied to the basal membrane, creating a pressure difference across the basal membrane. Since pressurizing the apical surface of the cell would cause the entire cell to be pressurized to the same amount, applying the pressure at the basal surface still accurately represents the apical pressure application *in vitro*.

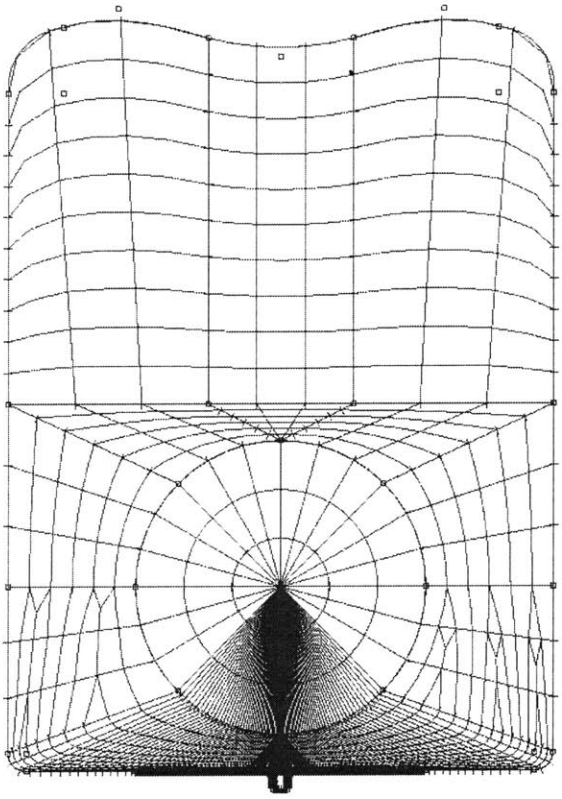

Figure 3.10: Mesh of a single epithelial cell attached to a porous membrane. The 0.4 μm pore is in the center of the membrane.

3.10.1 Pressure Model Results

A pressure difference of 2 kPa applied across the basal membrane of the epithelial cell model caused the cell to deform into the 0.4 μm pore in the substrate beneath the cell. Figure 3.11 depicts the effective stress near the pore. The nucleus, which is a factor of 10

stiffer than the cytoskeleton, contributes to the altered stress environment. Maximum effective stresses in the cytoskeleton, nucleus, and membrane were 12 Pa, 3 Pa, and 458 kPa, respectively. The maximum displacement into the pore was –0.05 μm. Cytoskeleton strain-ZZ was 8% in the center of the pore where the cytoskeleton is in tension, and 10% on the sides of the pore were the cytoskeleton is in compression (Figure 3.12). The region of increased stress was localized to a radius of approximately 0.5 μm from the center of the pore.

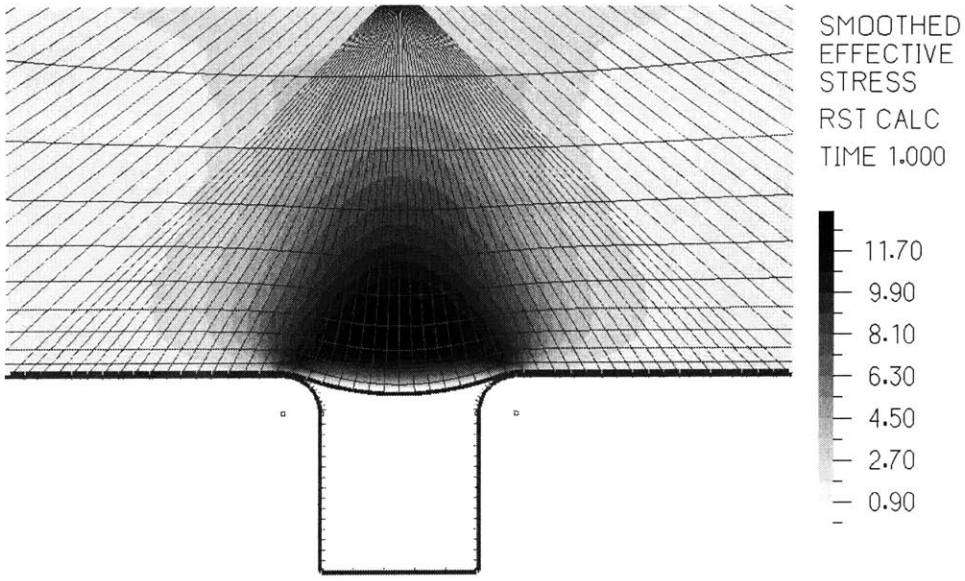

Figure 3.11: Pore model effective stress near the 0.4 μm pore.

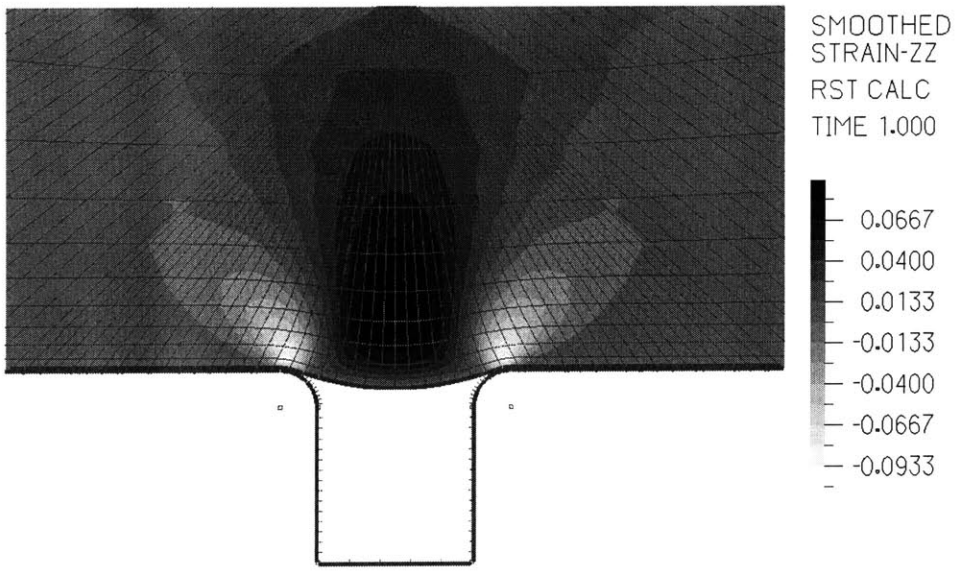

Figure 3.12: Strain-ZZ plotted near the 0.4 μm pore.

Table 3.1 shows the effects of increasing the transcellular pressure from 500 Pa to 2580 Pa. The membrane effective stress increases exponentially with the pressure (Figure 3.13) due to geometric nonlinearities arising from the increasingly large displacements and strains over 5%.

Membrane	Pressure (Pa)	500	1000	1500	2000	2580
	Effective stress (kPa)	215	331	415	458	499
	Stress-rr (kPa)	245	376	472	525	574
	Stress-tt	120	184	231	257	281
	Strain-rr	0.019	0.028	0.036	0.034	0.044
	Strain-ss	0.008	0.027	0.034	0.038	0.042
	Displacement-Z (μm)	-0.039	-0.047	-0.047	-0.051	-0.055
	Strain-ZZ	-0.055	-0.0569	-0.067	-0.078	-0.088
Cytoskeleton	Effective stress (Pa)	7.08	9.24	10.8	12.07	13.26
	Strain-ZZ	-0.055	-0.076	-0.089	-0.0099	-0.106
Nucleus	Effective stress (Pa)	1.8	2.2	2.6	3.17	3.16
	Strain-ZZ	-0.0051	-0.0067	-0.0078	-0.0027	-0.0094

Table 3.1: Effects of increasing the transcellular pressure.

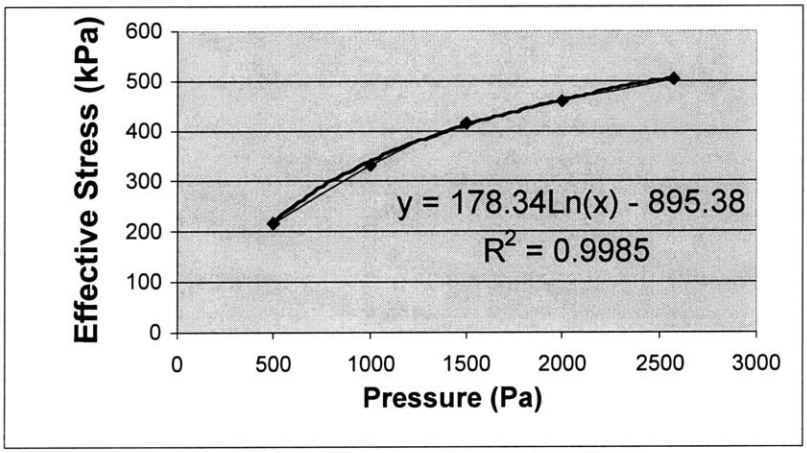

Figure 3.13: Increasing the transcellular pressure in the finite element program causes an exponential increase in the membrane effective stress.

Since the material properties of airway epithelial cells are still largely unknown it was important to determine which parameters would have the largest impact on the stresses and strains that the cytoskeleton, membrane, and nucleus are exposed to. Table 3.2 shows the effects of changing the material properties. Increasing the stiffness of the

cytoskeleton by a factor of 10 decreases membrane stress, but does not significantly affect membrane strain. Cytoskeleton effective stress is decreased from 12 Pa to 9 Pa and membrane displacement in the Z-direction at the pore decreases from 0.1 μm to 0.07μm.

Changing the membrane stiffness by a factor of 10 has a larger impact. Decreasing the membrane stiffness decreases the membrane effective stress by a factor of 3.5 and increases strain-rr, from 4% to 11%. Cytoskeleton stresses and strains are similarly affected. Cytoskeletal effective stress increases from 12 to 33 Pa and cytoskeletal strain doubles from 10% to 20% since stress is borne less by the membrane and more by the cytoskeleton. Increasing the membrane stiffness increases membrane stresses up to 1.3 MPa and decreases membrane strains to 1%. Cytoskeleton stresses and strains are also decreased due to reduced deformation in the vicinity of the pore.

	Pressure (Pa)	2000	2000	2000	2000
	Membrane Young's Modulus (Pa)	$E=10^7$	$E=10^7$	**$E=10^6$**	**$E=10^8$**
	Cytoskeleton Young's Modulus(Pa)	E=100	**E=1000**	E=100	E=100
Membrane	Effective stress(kPa)	458	450	132	1211
	Stress-rr (Pa)	525	515	153	1389
	Stress-tt (Pa)	257	252	747	680
	Strain-rr	0.034	0.039	0.116	0.011
	Strain-ss	0.038	0.038	0.111	0.010
	Displacement-Z (μm)	-0.051	-0.050	-0.107	-0.023
	Strain-ZZ	-0.078	0.077	-0.138	-0.025
Cytoskeleton	Effective stress (Pa)	12	9	33	5.1
	Stress-ZZ (Pa)	21	15	58	8.3
	Strain-ZZ	-0.098	-0.075	0.207	0.0399
	Displacement-Z (μm)	-0.05	-0.04	0.108	0.0232
Nucleus	Effective stress (Pa)	3	2.2	7	1.1398

Table 3.2: Effects of changing material parameters by a factor of 10.

3.10.1.1 Estimation of stress and tension

The membrane tension on the sides of the pore can be estimated from the hoop stress by assuming that the shape of the deflection is semi-circular (Figure 3.14). From the finite element results the effective radius of the deformation is 0.55 μm. Therefore, if the pressure difference across the membrane is 2 kPa, the tension in the membrane at the side

of the pore should be on the order of 0.0011 Pam. Since the membrane is 6 nm thick, the stress in the membrane should be approximately 183 kPa.

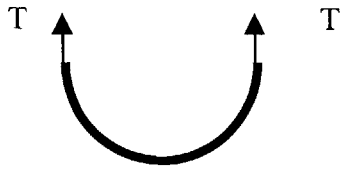

Figure 3.14: Idealized depiction of membrane tension at the side of the pore.

$$T = R\Delta P \cong .0011Pa * m$$
$$\sigma = 183{,}333Pa$$

The tension further from the pore on the basal surface of the cell can be estimated from a force balance assuming no shear stress. Seven microns from the pore, near the lateral wall, the shear stress should be around 5 kPa.

$$T = T_o \frac{R_o}{R} = .000031Pa * m$$
$$\sigma = 5238Pa$$

3.11 Fluid Model

The fluid model consisted of two elastic cells separated by a fluid filled intercellular space (Figure 3.15). A fluid-structure interaction analysis was performed in ADINA in order to determine if a transcellular pressure increases fluid flow in the intercellular space. Rigid struts spanned the upper 10 μm of the intercellular space, and isoparametric beam elements were used to model the fiber matrix of the ECM in the lower 50 μm of the intercellular space. The stiffness of the fiber matrix struts was determined to be 2 x 10^9 kPa based on the stiffness of actin. The fluid had a density of 1000kg/m^3 and a viscosity of 1 cP. For the analysis 9-node fluid elements were used and the flow was assumed to be laminar. 30 Pa pressure was applied to the apical surface of both cells and the basal surfaces were constrained the same as for the pore and bead model. The fluid/structure interface included the lateral walls of the intercellular space. The intercellular space was 0.2 μm wide for the apical 10 μm, and 0.5 μm wide for the basal 5 μm. In the remaining

5 μm of the intercellular space there was a reservoir with a maximum width of 2.7 μm at center of the reservoir.

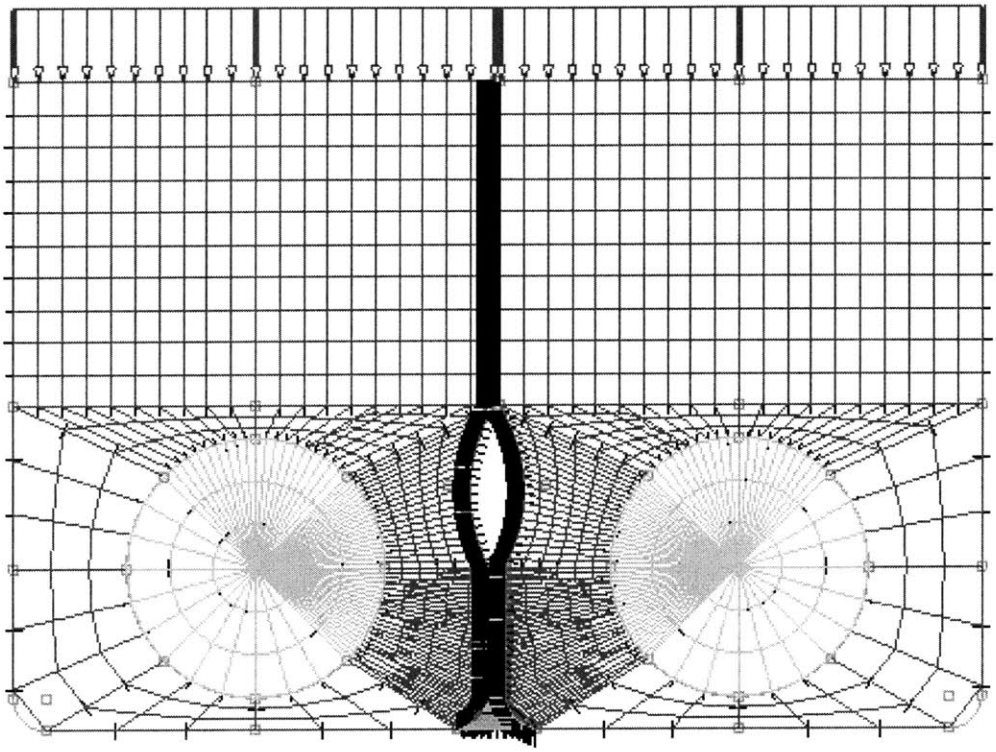

Figure 3.15: Fluid mesh before pressure application. The thick black lines represent the fluid-structure interaction. The light gray circles represent the nuclei.

3.11.1 Fluid Model Results and Discussion

The results for the fluid model are shown in Figure 3.16. When the two epithelial cells were pressurized with only 10 Pa, the reservoir in the intercellular space narrowed by 0.4 μm, from an initial width of 2.7 μm. A maximum effective stress of 10 Pa occurred at the top of the reservoir and an effective stress of around 5 Pa surrounds the reservoir. Interestingly, the nucleus also experiences an effective stress of around 5 Pa. Since only a fraction of the actual pressure caused the intercellular to narrow and the cytoskeletal stresses to increase, it can be anticipated that 2 kPa of pressure could potentially cause much larger deformation with considerably higher stresses.

The parameters used in the fluid model were largely speculation and they were meant to determine if increased shear stress in response to pressure application could be of a

magnitude large enough to elicit a biological response. However, since so many parameters were unknown, we decided to pursue imaging techniques to provide data to use in the fluid finite element model and to verify that the intercellular spaces collapsed with an increased pressure. Contrary to what we first believe the imaging results, discussed in detail in the following chapter, appeared to show that the intercellular spaces did not collapse, but widened. Due to the unexpected results, the fluid finite element model was abandoned until more information could be determined.

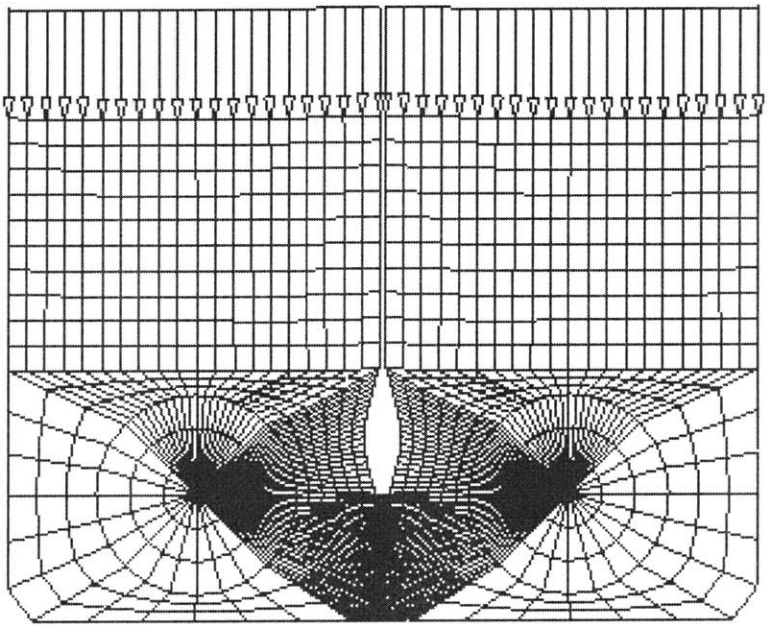

Figure 3.16: Fluid mesh after pressure application. The reservoir width has decreased.

3.12 Finite Element Discussion

The finite element models presented here indicate mechanosensory pathways that could lead to the upregulation of Egr-1 and the activation of ERK. The bead model shows maximal stresses in the vicinity of the bead, but also increased stresses throughout the cell layer. The pressure model shows increased stresses due to deformation into the pore. The models had a wide range of maximum effective stresses ranging from 10 to 100 Pa. In the bead model, the maximum stress was over 100 Pa, but concentrated in a small area to the left of the bead. Effective stresses in the bead model were around 10 Pa to a distance of 4 μm from the bead. In the pore model the area of highest stress was

confined to a 0.5 μm radius from the pore. The fluid model showed stresses of 10 Pa to small areas to either side of the top of the reservoir. All the models showed increased stresses in nucleus.

These finite element results suggest that cytoskeleton stresses are on the order of 10 Pa, potentially large enough to initiate a biological response, so that localized conformational changes could play a significant role. Membrane strain in each of the models was high, up to 500 kP, and could stimulate strain activated ion channels, or even displace membrane-spanning integrins and perturb the cytoskeleton enough to elicit a biological response.

The finite element models presented here are simplified and can be updated as more information is discovered about the mechanical properties of epithelial cells. However, since asthmatic airway epithelial cells are in an altered environment they may have material properties dissimilar from other epithelial cells in "normal" environments. Many studies have shown that epithelial cells in asthmatic airways have abnormal histology with epithelial inflammation (21). Abnormal mechanical properties may contribute to an altered response to mechanical force and to other stimuli.

Finite element results are useful to indicate areas where increased stresses could cause mechanostimulatory events. The results presented here are useful for suggesting pathways to consider in more detail. Deformation into the porous substrate and collapse of intercellular spaces are two mechanisms that increased stresses in these models, indicating that they should be looked at in more detail. For this reason, we decided to employ imaging techniques to provide more information as to the feasibility of these mechanisms. With new information, the mathematic models can be modified to represent the physical system more accurately.

Chapter 4
Imaging

Imaging cells in their *in vitro* or *in vivo* environment is a valuable way to observe how cells respond to mechanical challenge. Many imaging techniques exist and we chose two, in addition to light microscopy, to investigate how the morphology of bronchial epithelial cells change when the cells are exposed to a transcellular pressure difference. The first imaging technique, transmission electron microscopy (TEM) was chosen to image the airway epithelial cell layer morphology before and after pressure application. The second imaging technique, two-photon microscopy was chosen for its improved resolution in the axial and lateral dimension, low photobleaching capacity, and because living cells can be imaged during pressurization. Light microscopy was used to verify the confluence of the cells, and to aid in the two-photon microscopy tests.

This chapter begins with a review of imaging techniques used in a variety of studies to measure and observe lateral intercellular spaces (LIS) and fluid flow in epithelial cells. Then the TEM studies performed are described along with a discussion of the results. A detailed description of the two-photon microscope principles, setup, and techniques for imaging the cells before and during pressure application follows. Each of the fluorescent dyes used is described along with the preparation methods. This chapter ends with the two-photon results and limitations, and a discussion of what the results suggest about mechanosensory pathways in pressurized airway epithelial cells.

4.1 Review of Previous Imaging Tests

Previous studies have measured the dimensions and characteristics of intercellular spaces as well as water permeabilities across cell layers using a variety of imaging techniques. However, for some imaging modalities artifacts arise from fixation techniques. Initially, scanning electron microscopy (SEM) studies revealed dilated intercellular spaces in cell systems. However, it was later shown that dilated intercellular spaces arise from SEM fixation and embedding and that light microscopy does not reveal dilated intercellular spaces (14).

Spring et al (50), used a novel light microscopy method as an alternative to SEM to determine the size and compliance of the intercellular spaces in gallbladder epithelium.

The goal was to show that dilation of the intercellular spaces as seen in SEM images was not an artifact due to fixation, but rather the final path for fluid transport. The lateral intercellular space width during fluid transport ranged from near 0 μm at the tight junction to an average of 1.343 ± 0.215 μm near the basal surface. Spring also noticed that fluid filled pools occurred most frequently when three cells came together. He determined that the spaces collapsed when fluid flow ceased and increased when fluid flow resumed and when a pressure of 5 cmH_2O was imposed at the basal surface. Spring hypothesized that the intercellular space may increase with an applied pressure due to more fluid entering from the apical surface and to a pressure-induced blockade at the basal surface preventing fluid from leaving. It was also determined that the high compliance of the lateral intercellular space walls allowed for large deformations of the same magnitude for both pressurized cells and those with active fluid transport.

Confocal microscopy has also been used to analyze intercellular spaces and fluid transport in epithelial cells. Kovbasnjuk et al. (26) used confocal microscopy to show that fluid does not flow across the tight junctions of renal epithelium. By reducing the pore size in the substrate and then microinjecting fluorescein dextran between the substrate and the cells that was too large to pass through the pores, the concentration gradient and volume flow in the intercellular spaces was determined. The two dyes used were 3 mM 70,000 molecular weight (MW) fluorescein dextran and 2 mM 3000 MW BCECF. Iterative deconvolution was performed on the images in order to measure the intercellular spaces. LIS width ranged from approximately 0.55 μm near the tight junction to almost 1 μm, 6μm below the tight junction, and the lateral intercellular space volume per cell was 46 fl. The diffusion coefficient for 70,000 MW dextran in cell systems grown on permeable supports was determined to be 1×10^{-7} cm^2/s. Under control conditions the volume flow rate at the tight junction was -0.036 $nl/cm^2/s$. With a 28 mOsm apical osmotic shock the volume flow rate increased to -2.089 $nl/cm^2/s$, but the cross-sectional area of the spaces did not change. The results from the study indicate the intercellular spaces are relatively hypertonic, causing fluid to enter the LIS from the adjacent cells by osmosis. Since the intercellular spaces are limited in their distensibility fluid is forced to flow out of the intercellular spaces at the basement membrane.

Matsui et al. (30), used confocal microscopy to determine osmotic water permeabilities in human bronchial epithelial (HBE) cells. Pseudostratified airway epithelial cells were grown on a flexible permeable filter and stained with 3 mM Calcein, AM. The filter was placed on spacers in a bath of Texas Red stained TES buffered Ringer's solution. Cell layer height and the Texas Red fluid bath fluorescent intensity and height were measured by imaging in the XZ-plane. From height and fluorescent intensity measurements the osmotic water permeability in response to osmotic shock directed at the apical or basal surface were calculated. The transepithelial osmotic water permeability in HBE cells was 168.6 ± 24.3 μm/s, and the transapical osmotic water permeability was 1.2 ± 0.03 μm/s. The transbasolateral osmotic water permeability is significantly lower than the transapical permeability. The authors concluded that normal and cystic fibrosis airway epithelial cells both have high water permeabilities and that together the tight junctions and lateral intercellular walls are the limiting factor in water flow across the cell layers.

Finally, TEM has been used extensively to characterize the morphology of cell layers and of intercellular spaces. Filippatos et al., used TEM to determine the morphology and the existence of tight and adherens junctions in primary alveolar epithelial cells (13).

4.2 Transmission Electron Microscopy

Since TEM has proved effective in imaging epithelial cells and intercellular spaces, we decided to use it to verify the confluence and the pseudostratified nature of our epithelial cell layers. From the images we were also able to obtain geometric measurements for average length, height, and area of the epithelial cells and the shape of the nucleus. The resolution at the sub micron level, depth of field, availability of equipment, and success in previous studies make TEM an ideal imaging technique.

4.2.1 TEM: Methods

Cells in 24 mm Transwell inserts were pressurized for 30 minutes using the pressure apparatus previously described in chapter 2, and lysed. Non pressurized cells were also lysed for comparison. All samples were fixed and processed, and then sliced into 30-60 nm trapezoid sections using a RMC MT6000 ultramicrotome (RMC, Inc. Tucson, AZ).

Each trapezoid section was placed on a grid and imaged with a LEO902 energy filtering transmission electron microscope (LEO Electron Microscopy, Inc., Thornwood, NY).

4.2.2 TEM: Results

With TEM we were able to verify the pseudostratified nature and the confluence of the cell layer (Figure 4.1) as well as determine height of the cells and average diameter of the nuclei. The average height of the cell layer was 22.18 ± 2.49 μm and the average radius of the nucleus was 3.31 ± 2.23 μm^2. However, due to the 2D nature of the images, the value for the radius of the nucleus will be an underestimate.

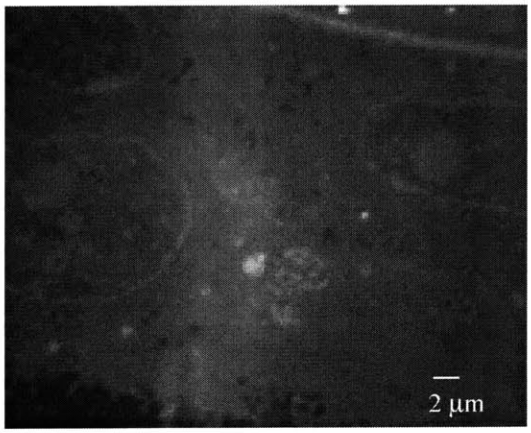

Figure 4.1: TEM of cell layer.

At the basal surface pseudopods were observed in the pressurized cell samples. It appears that the pseudopods extend into the 0.4 μm pores beneath the cells, since the pseudopods are also 0.4 μm wide. However, TEM imaging requires the cells to be lysed, fixed, cut into micron thick slices, and embedded, so the images may not accurately represent the cell morphology. Every pseudopodium seen in this study was along side a large circular hole that is most likely caused by cutting the samples into ultra thin slices. In some samples the entire cell layer became detached from the substrate. Figure 4.2 shows a cellular protrusion into the pore as well has a hole in the substrate, most likely created during the cutting procedure. To date we have not been able to verify that the pseudopod is actually deforming into a pore and not into a defect in the membrane. Pseudopod formation into the pores was only seen in pressurized cell layer, which suggests that the pressure may stimulate or cause deformation in the porous substrate.

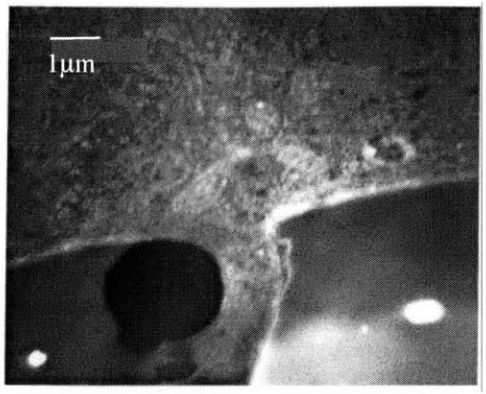

Figure 4.2: TEM of a pseudopod extending from the basal surface of a pressurized airway epithelial cell. A hole in the substrate can be seen to the left of the pseudopod.

The TEM images showed that the intracellular spaces between the cells consist of regions of close apposition, which are most likely tight and gap junctions, and wider spaces that we refer to as reservoirs. The tight junctions were localized near the apical surface while the reservoirs were interspersed throughout the basal layer of the cells. Finger-like protrusions from the cells extend out into the wider spaces.

In addition TEM also showed an increased number of mucous vesicles in the pressurized epithelial cells. Figure 4.3 depicts mucus vacuoles near the apical surface, a number of vacuoles actively releasing mucus, and mucus above the cells. Mucus hypersecretion and metaplasia are trademarks of asthma, contributing to airway obstruction and amplifying smooth muscle constriction (10). It can be suggested from our TEM images that constriction of the airways promotes remodeling through increased mucus production and release.

Figure 4.3: TEM of Mucus vacuoles released from the apical surface of pressurized airway epithelial cells.

4.3 Two-Photon microscopy

Two-photon microscopy was employed to dynamically visualize the cells before, during, and after pressurization. It is an ideal method for imaging cells because of its enhanced depth discrimination and noise rejection, and its ability to reduce photobleaching.

In two-photon microscopy a fluorescent chromophore is excited by the simultaneous adsorption of two incident long-wavelength photons in the infrared range. Each photon has half the energy needed to excite the chromophore. The need for two photon activation gives rise to a highly localized region of fluorescence since two photon excitation has a lower probability of occurring compared to one photon excitation (confocal microscopy). Excitation of the chromophore photons is achieved by the use of very high peak power produced by a femtosecond pulsed laser. The combination of the excitement of small regions and the use of long-wavelength photons instead of UV light lessens the amount of photobleaching, common in many other imaging modalities.

4.3.1 Two-Photon Experimental Apparatus

A two-photon scanning fluorescence microscope was previously configured in Prof. Peter So's lab at MIT and all two-photon data collected as part of this project was done with the help of doctoral candidate Lily Hsu. A schematic of the two-photon system is detailed in Figure 4.4 and a detail review can be found in reference 47. Briefly, an Argon-Iron laser (Innova 310, Coherent Inc., Palo Alto, CA) pumps a mode-locked Titanium-sapphire laser (Mira 900, Coherent Inc., Palo Alto, CA). The Ti-sapphire laser has a high average power of 1.5 W, a high repetition rate of 80 mHz, and a short pulse width of 150 fs. The wavelength was tuned to 780 nm, which was in the range of probes used for this study. The laser light is enters the microscope via a galvanometer driven X-Y scanner (Cambridge Technology, Watertown, MA). A dichroic mirror (Chroma Technology, Inc., Brattleboro, VT), which is a custom-made short pass filter, reflects the excitation beam directed by the scanner into the objective. A 63X water Zeiss Fluar objective with an aperture of 0.9 is used because of its high aperture and throughput. The formation of a diffraction limited point spread function arises from the high aperture.

A polarizer and quarter-wave plate between the lasers and the scanners attenuates the laser power and changes the linear polarization of the laser light to circular. Attenuation is crucial to limiting the amount of the incident power to which the sample is exposed. A custom-built interface circuit allows the computer to control the X-Y scanner, which scans at a maximum rate of 500 Hz. The pixel residence time during scanning is optimized to reduce photon noise. A computer interfaced piezoelectric nanopositioner (PI Inc., Auburn, MA) moves the objective in the axial direction. The objective can image to a depth of 100 μm and the axial resolution is approximately 0.08 μm.

Fluorescence from the excited chromophores passes back through the objective and the dichroic mirror and is attenuated by a barrier short pass filter (BG39 Schott glass, CVI Laser, Livermore, CA). The filter eliminates most of the residual scatter and is specific for the fluorescent spectrum of the probe being used so that fluorescence is minimally attenuated. A de-scan lens directs the light into the photo multiplier tube (R5600-P PMT, Hamamatsu, Bridgewater, NJ), where the fluorescence at each pixel is collected. In the PMT the number of single photons is counted and then transferred to the computer where the optical section images are displayed.

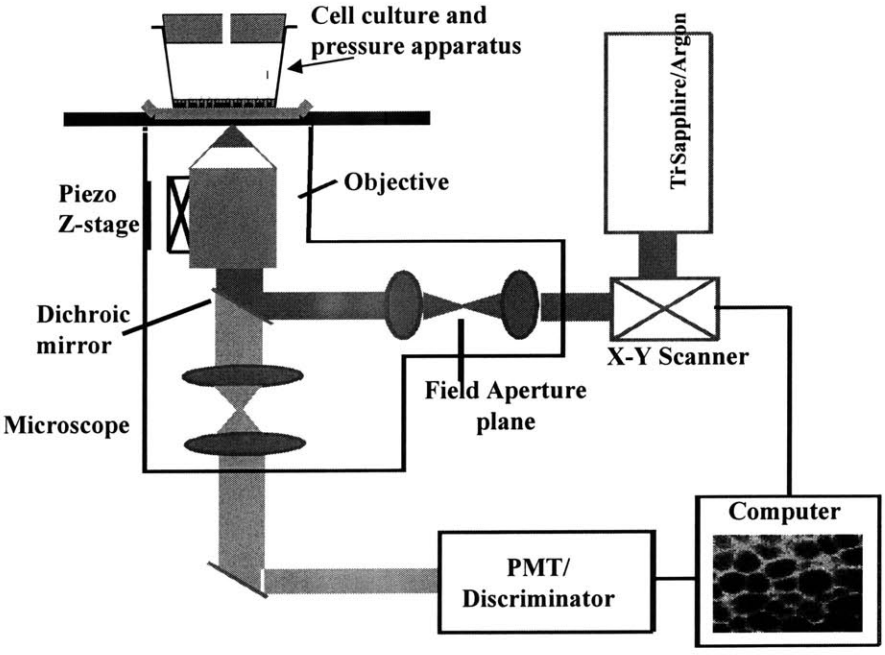

Figure 4.4: Two-photon schematic. (So, Kochevar, 1998)

4.3.2 Sample Preparation

Bronchial airway epithelial cells were cultured on 12-mm Transwell filters as previously described. Approximately two weeks after forming the air-liquid interfaces the cells reached full maturity and were ready to be imaged. The day before imaging, the cells were transported from the Pulmonary Division Research Laboratory at the Brigham and Women's Hospital to the imaging lab at MIT. The cells equilibrated overnight in an incubator with 5% CO_2: 95% air at 37°. A live/dead stain (LIVE/DEAD Viability/Cytotoxicity Kit, Molecular Probes, Eugene, OR) test was performed to verify the viability of the cells after transportation. Results showed one dead cell among thousands plated on the Transwell filter. The live stain was 4 mM Calcein, AM in anhydrous DMSO and the dead stain was 2 mM Ethidium homodimer-1 in DMSO/H_2O. The staining was performed in accordance with the protocol suggested by Molecular Probes (Appendix 1). The solvent used was phosphate buffered saline (PBS) at pH 7.4.

Before staining the cells were visually inspected with a light microscope to verify confluence. Then, one Transwell at a time was stained bilaterally with a fluorescent probe. Calcein, AM, and fluorescein, RhodamineB, and BCECF conjugated dextrans at various molecular weights were all used separately to stain the epithelial cells. The reasons from choosing each probe is described in detail in a following section.

To stain the cells, 0.5 μL of Calcein, AM (1mg/mL solution in dry DMSO, Molecular Probes) was added to 1 mL of PBS at a pH of approximately 7.4. The solution was vortexed to insure adequate mixing. The final solution was 1 mM Calcein, AM. In a new sterilized tray, 75 –200 μL of Calcein, AM solution was pipetted into a plate well, and the Transwell filter with differentiated cells was placed in the well on top of the solution. A visual inspection was performed to insure that the entire bottom surface of the cell layer was exposed to the Calcein, AM. Then 25-100 μL of the Calcein, AM solution was pipetted onto the apical surface of the cells. The cells were removed from the incubator immediately prior to staining. All solutions were at room temperature when added to the cells.

To stain the intercellular spaces a similar protocol was used. 10,000 and 70,000 MW fluorescein, RhodamineB, and BCECF conjugated dextrans were all used in concentrations ranging from 3 μM to 3 mM in PBS. Again, 75 – 200 μL of the dextran

solution was pipetted underneath the filter, and 25-100 μL was pipetted on top of the cell layer. The fluid layer on top of the cell layer was approximately 1 mm thick.

The cells were incubated at room temperature in the dark for 45 to 60 minutes, based on the protocol suggested by Molecular Probes. Before imaging, excess solution was pipetted off the apical surface while taking care not to touch the pipette to the cell layer. The fluid was removed in order to replicate the previous cell culture test without adding new variables. A thin layer of fluid was left on the apical surface of the cell to prevent drying out and to provide a fluorescent marker for the top of the cells.

4.3.3 Probes

A variety of probes were chosen to stain the 12 mm wells of airway epithelial cells. Fluorescein, BCECF, and RhodamineB dextrans, Texas Red, Laurdan, and Calcein, AM were all tried in a wide range of molecular weights. All probes were obtained from Molecular Probes (Eugene OR) except for the 200,000 MW fluorescein dextran, which was obtained from Sigma-Aldrich (St. Louis, MO).

4.3.3.1 Dextrans

Dextrans are biologically inert non-toxic molecules that are ideal for imaging. Dextran is a hydrophilic and highly water-soluble polysaccharide that can be used in conjunction with a fluorescent molecule in order to help localize the fluorescent molecule in a cellular system. Dextrans are available in a wide range of molecular weights ranging from 3000 Daltons to 2,000,000 Daltons. Because dextran is not degraded by most endogenous endocellular glycosidases, dextran conjugated dyes are more permanent than free dyes, which is optimal for longer scan times. We found that the smaller molecular weight (MW) dextrans, including 3,000 and 10,000 Dalton dextrans diffused into airway epithelial cells (Figure 4.5). The 70,000 MW dextrans all appeared to be cell impermeant, and only stained the intercellular spaces. Staining the intercellular spaces and not the cell interior is referred to as negative staining. For all 70,000 MW dextrans produced by Molecular Probes there are 3-8 dye molecules per dextran. The wavelength spectrum for the dextrans used is listed in Table 4.1, and graphed in Figure 4.6. BCECF, Fluorescein, and RhodamineB dextrans were all chosen because the wavelengths they fluoresce at are ideal for the two-photon microscope previously described.

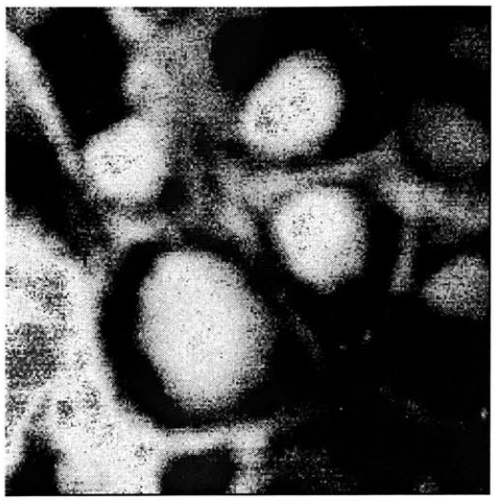

Figure 4.5: Human airway epithelial cells stained with 10,000 MW BCECF dextran.

Most of the dextrans come in vials of 25 mg of powder, which must be stored at –20°C. Immediately prior to staining, 120 μL of PBS was pipetted into a vial of the conjugated dextran power and vortexed to insure mixing. 50 mg of conjugated dextran was used per sample. The cells were exposed bilaterally to the dextran solutions as previously described. Theoretically, the dextran dyes would not be able to pass through the tight junctions at the apical surface of the cell layers because of their size. The majority of the solution most likely enters basally though the substrate where it is diffusion limited by the pores. Once the dye reaches the cell layer is can enter into the basal opening up the intercellular spaces.

Spectra	Abs (nm)	Em (nm)
BCECF	508	532
Fluorescein	494	521
RhodamineB	570	590

Table 4.1: Wavelength spectrum for dextrans conjugated dyes used in this study.

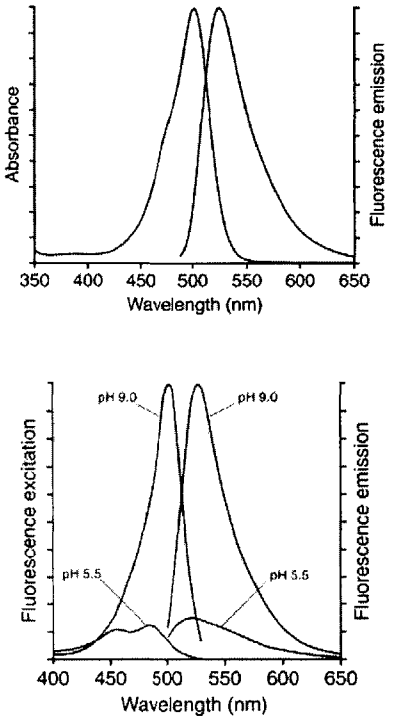

Figure 4.6: Wavelength profile for A) fluorescein and RhodamineB dextrans and b)BCECF dextran. Courtesy of molecular probes.

Fluorescein is intrinsically anionic and it is cell impermeant at higher molecular weights. RhodamineB is zwitterionic or neutrally charged and is cell impermeable in some cell types. 2',7' –bis-(2-carboxyethyl)-5-(and-6)-carboxyfluorescein (BCECF) is a polar molecule that is highly pH dependent. BCECF has excellent intracellular retention although it is strongly pH dependent. All have proven successful in previous studies (5).

4.3.3.2 Calcein

Calcein, AM is membrane permeant and is hydrolyzed by endogenous esterases inside the cell. Once hydrolyzed Calcein becomes a negatively changed green fluorescent molecule, ideal for imaging the cytoplasm inside the cell. However, over time some of the activated form of Calcein can leak out of the cells and into the intercellular space. Calcein is loaded into the cells non-invasively, has superior cell retention, is pH independent, and has been used by others studies in order to determine the change in height of the cell layer (30).

4.3.3 Image Acquisition

After incubation, the cells were loaded into the two-photon microscope. 100 μL of staining solution was pipetted onto the imaging cover slip and the Transwell filter holding the cells was placed on top of the bolus of solution. The schematic in Figure 4.4 shows the location of the Transwell filter in the microscope schematic. Before loading onto the microscope, the rubber stopper from the pressure apparatus was pressed into the top of the Transwell filter. Then the Transwell filter was placed on the cover slip and held in place by two metal clamps. A pressure tank with 5% CO_2: 95% air was directly connected to a manometer and the pressure was adjusted to 30 cmH_20. The pressure was allowed to stabilize before pressurizing the cells.

Once the cells and the pressure apparatus were in place, manual adjustment knobs were used to move the objective directly beneath the center of the Transwell filter. A drop of water was pipetted between the water lens of the two-photon microscope and the cover slip and the stage light was turned off. A black sheet covered the microscope to block all outside light.

Collected images were 256 x 256 pixels and one pixel was equivalent to 0.144 μm. Images were acquired every 0.2 μm in the +z-direction starting from the membrane. The cell layers were around 30 μm thick. Each image could be obtained in 7 seconds and one complete image stack took 20 to 30 minutes.

After a sequence of images was taken for an unpressurized cell layer the cells were pressurized and the imaging process was repeated. The z-stage was manually adjusted to compensate for the downward movement of the substrate when it is exposed to the pressure difference. Throughout the scan the pressure was monitored and adjusted to maintain a constant 30 cmH_20.

4.3.4 Post-processing

Images taken by the two-photon microscope are convolutions of the actual image and a point spread function (PSF) inherent to the microscope. The PSF is the out-of-focus haze created by the circular aperture of the microscope. Deconvolution was performed with AutoDeblur (AutoQuant Imaging, Troy, NY), which uses the Constrained Maximum Likelihood Estimation Theory to determine the PSF.

Before deconvolution, each image stack was opened in Spyglass Slicer (Spyglass, Champaign, IL). Slicer provides volumetric rendering of a sequence of image slices. Figure 4.8 in the following section depicts a Slicer image stack with the cell, substrate, and fluid layers labeled. The cell layer height was computed by counting the slices from the substrate on the basal surface to the fluid on the apical surface. After deconvolution, the images were again visualized with Slicer to inspect the images and the morphology of the cells throughout the layer. Only stacks with clear intercellular spaces of the same cell section before and during pressure application were chosen. In some cases the images could not be used because the sample shifted in the x- or y-direction when pressurized, so that different cell sections were imaged before and during pressure application.

IMOBJ, a customized software program used to view and manipulate 2D data, was used to rasterize individual slices. In IMOBJ intensity levels for each slice were normalized between 0 and 1 and adjusted to remove background noise. Matching slices (at the same height in the cell layer) before and during pressurization were then opened in Scion Image (Frederick, MD) to measure intercellular space widths and areas. The scale was set to 0.144 μm/pixel. To measure intercellular space width, a line was drawn across the intercellular space and the intensity profile was plotted as in Figure 4.7. The full-width half-maximum values, indicated by the dark line, were recorded. The difference between the two values was taken as the intercellular space width at that position.

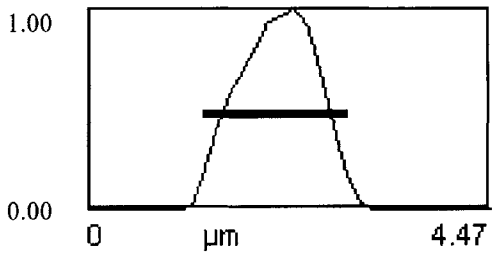

Figure 4.7: Intensity plot.

The total area of an image slice occupied by the lateral intercellular spaces was also measured. Using Scion Image thresholding was used to distinguish the intercellular spaces. The total area of an image that was above a predetermined threshold value,

signifying the LIS, was calculated. LIS area values were compared between slices in pressurized and non-pressurized stacks.

4.3.6 Two-Photon Results

4.3.6.1 Effectiveness of the Probes

The effectiveness of the probes varied depending on molecular weight, type of fluorescent molecule, batch of cells, dye concentration, and incubation time. As mentioned previously, 3000 and 10,000 MW probes appeared to enter the cells and stain the nuclei. 200,000 MW dextran did not stain the intercellular spaces effectively, suggesting that the dextran molecules were too large to enter the intercellular spaces. 70,000 MW BCECF dextran appeared to be cell impermeant and stained the intercellular spaces. 70,000 MW RhodamineB dextran appeared to diffuse into the cells in at least one sample and 70,000 MW fluorescein gave a high signal, but also high background noise. There is some concern about whether or not the 70,000 MW conjugated dextrans reached equilibrium during the incubation time and it will need to be addressed in future studies. For all 70,000 MW dextrans, 1-3 mM concentrations were effective.

In order to determine if the 70,000 MW dextrans crossed the tight junctions one cell culture was incubated with 70,000 MW dextran only on its apical surface. PBS was used as a buffer between the Transwell filter and the cover slip to prevent the cell layer from drying out. Two-photon images showed that the intercellular spaces were not stained even after transcellular pressurization. Six additional cell layers were imaged without any dye to determine the autofluorescence of the cells. The autofluorescence was minimal compared to the fluorescence of the dextran and calcein stains.

Calcein, AM gave mixed results. In some samples, the cells were stained effectively and the dye-free intercellular spaces could be measured. In other samples, the intercellular spaces were indistinguishable from the cells, or the Calcein, AM did not stain the cells. Some of the Calcein, AM may have lost its fluorescence after being in suspension for an extended period of time.

4.3.6.2 Change in Height

The height of the cell layer, from the substrate below the cells to the fluorescent layer on top of the cells, was determined as previously described. Figure 4.8 depicts 3D Slicer renderings of two image stacks before and after pressure. Green represents the epithelium, red signifies the fluorescent fluid bath on top of the cells, and blue depicts the substrate The average height of the cell layer decreased by 3.43 ± 2.49 μm from an initial height of 21.65 ± 6.11 μm (Table 2) when the cells were pressurized, showing that the pressure compresses the cell layer.

The thickness of the fluorescent fluid layer above the cells (red in Figure 4.8) was measured to show if fluid passed into the cells. After the application of 30 cmH_2O, the fluid layer decreased by 6.25 ± 4.68 μm. The large standard deviation shows that there was a wide range in the change in the fluid layer height with pressure. The reason for the variation is not clear, but may be contingent on the confluence and viability of the cell layer and the leakiness of the tight junctions, as well as on compliance of the lateral walls and the degree of fluid impedance at the basal surface.

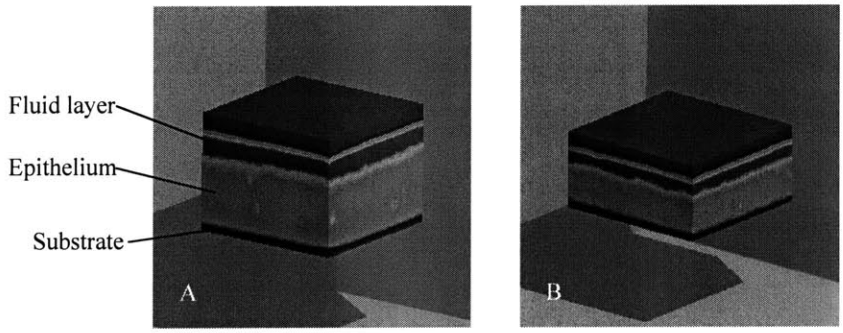

Figure 4.8: Change in cell layer height. A) Initial cell layer before pressure application. B) During application of 30 cmH_2O. Green signifies the epithelium, red represents the fluorescent fluid bath on top of the cells, and the blue along the basal surface of the epithelium is the substrate. (Images from Spyglass Slicer).

	Thickness before pressure (μm)	Thickness during Pressure (μm)	Change (μm)
Average	21.65	18.38	3.43
Standard Deviation	6.11	5.74	2.49

Table 4.2: Average change in cell layer thickness (n=18) for all cell layers regardless of fluorescent stain. (Values determined from Scion Image)

4.3.6.3 Change in Intercellular Space Width

Pairs of two-photon images taken before and during pressure application were compared. Table 4.3 lists the average change in width in microns of the intercellular spaces. For 70,000 MW BCECF stained cells the intercellular spaces increased 0.379 ± 0.154 μm. Calcein, AM stained samples increased 0.315 ± 0.024 μm, and 70,000 MW RhodamineB stained samples increased an average of 0.338 ± 0.236 μm. The agreement in the change in intercellular space width shows consistency between the different stains.

	Change in LIS width (μm)	**Standard Deviation**
BCECF dextran	0.379	0.154
Calcein, AM	0.315	0.024
Rhodamine, B	0.338	0.236

Table 4.3: Average intercellular space width change for airway epithelial cells stained with BCECF and RhodamineB dextrans, and with Calcein, AM. (Values determined with Scion Image)

Visual inspection of the images showed an increase in the intercellular spaces stained with BCECF dextran (Figure 4.9), Calcein, AM (Figure 4.10), and RhodamineB dextran (Figure 4.11) before and during pressure application. Large high intensity pools are seen where three or more cells come together. Some of the images might have shifted in the xy-plane after pressure, but common cells, before and during pressure application, can be distinguished. Figure 4.12 depicts the average intercellular space width for two image pairs starting around 7 μm up from the basal surface of the epithelial cell layer. The intercellular spaces were well defined in the middle of the cell layer. The graphs show a significant increase in LIS width during pressure application, however, the change is not always constant moving from the basal to the apical surface. Different magnitudes of intercellular width change are attributed to increased pooling in certain areas of the LIS. Before pressure application, the LIS widths were less than 1 μm. During pressure application, the widths range from 0.8 μm near the apical surface to 1.6 μm near the basal surface.

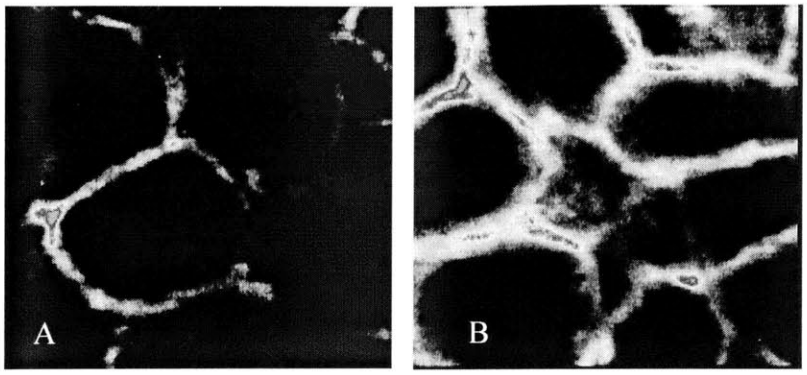

Figure 4.9: Airway epithelial cells stained with BCECF dextran. A) Before and B) during pressurization. (IMOBJ).

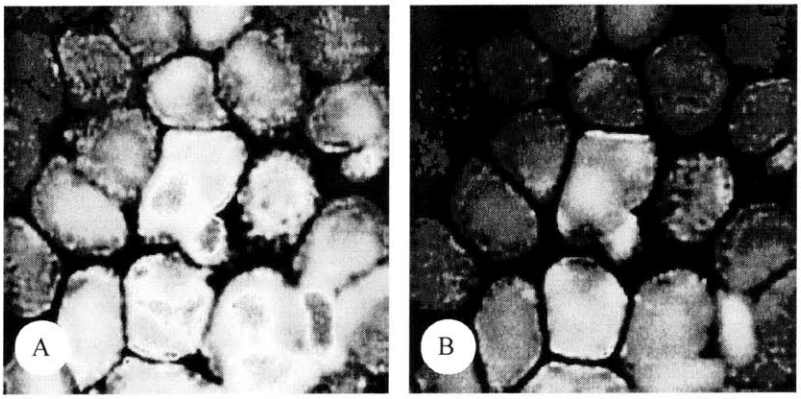

Figure 4.10: Airway epithelial cells stained with Calcein, AM. A) Before and B) during pressurization. (IMOBJ)

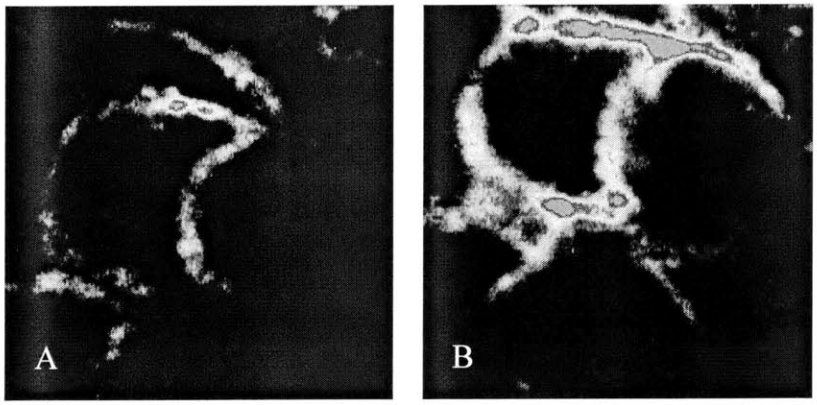

Figure 4.11: Airway epithelial cells stained with RhodamineB dextran. A) Before and B) during pressurization. (IMOBJ)

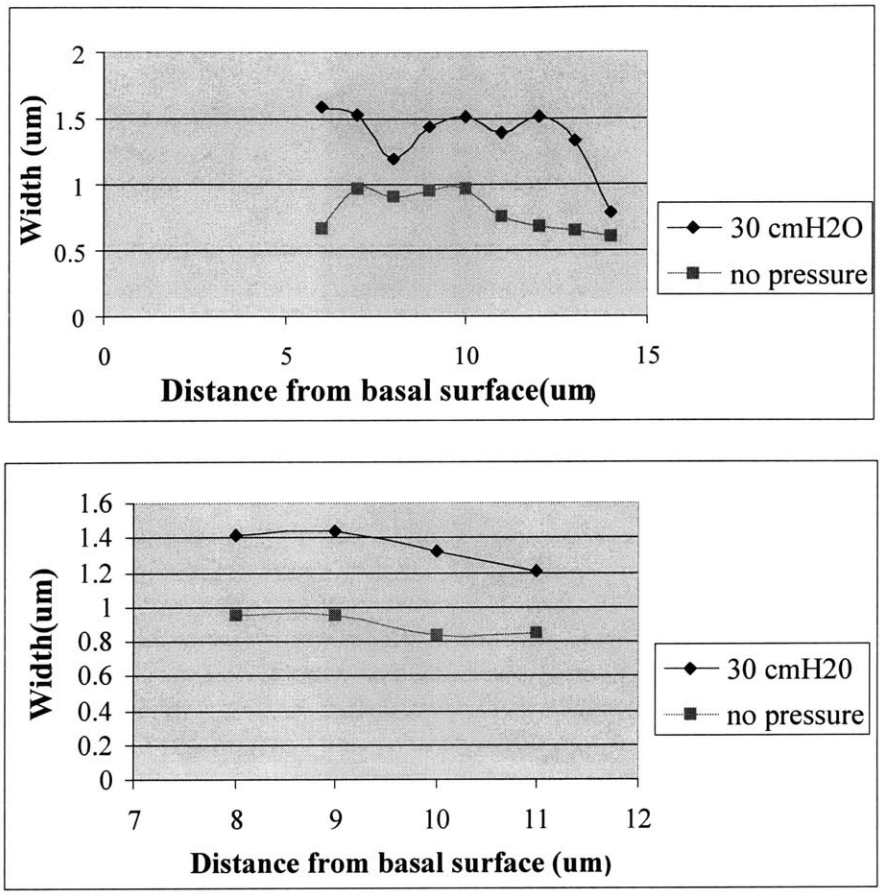

Figure 4.12. Average intercellular space width for two separate pairs of images measured using Scion Image.

The width of the intercellular spaces presented here is within the range determined by Kovbasjunk in a study described previously (26) using confocal microscopy. However, in the present study, there was not a steady increase in LIS width from the tight junctions to the basal level of the cells as seen by Kovbasjunk. Part of this discrepancy may be due to the morphology of the cell layers. Renal epithelial cells typically grow in a monolayer, while the airway epithelial cells differentiate into a pseudostratified layer, making the LIS more tortuous.

While we had anticipated a reduction in cell height due to loss of fluid through the basolateral membrane, the increase in separation distance between the cells was not expected. One hypothesis is that pressurizing the cell layer causes the basal surface of the cells to deform into the pores in the substrate, essentially creating a seal at the rim of the pore and trapping the fluid. Finite element modeling showed increased stresses at the sides of the pores, which could contribute to a plugging effect similar to a diaphram seal.

Fluid can enter the intercellular space through a number of ways. It is likely that fluid does not cross the tight junctions, but instead enters the cells at the apical membrane and exits the cells at the basolateral membrane(49). If the pores in the substrate are sealed then fluid cannot exit the cell layer, and may accumulate in the LIS over time.

4.3.6.4 Change in Intercellular Space Area

In order to determine if the intercellular space volume changed with pressure, the total intercellular space area per image was measured from intensity values as previously described. LIS area increased by approximately 400 μm^2 per image for the BCECF dextran and Calcein, AM stained cells when the cell layers were pressurized with 30 cmH_2O. The change in intercellular space area for two samples is depicted in Figure 4.13. The LIS area increased from basal to apical surface, which could be due to increased pooling, higher intensity values occurring after prolonged diffusion time, or a decrease in the viability of the cell layer. It typically took 30 minutes to complete a scan. Before pressure application, the LIS area appeared to be constant over the height of the cell layer. Figure 4.14 shows a pair of 70,000 MW BCECF dextran stained cells. During pressure application there is a significant increase in intercellular space area and a large fluid accumulation where three cells come together. Increased pooling can also be attributed to plugging at the substrate pores, preventing fluid from leaving the cell layer as mentioned above.

The LIS volume, V_{LIS}, can be calculated from the area measurements. Each image is 244 x 244 pixels after deconvolution, which is equivalent to 35 x 35 μm. The surface area of the Transwell filter, S_T, is 1.13 x 10^8 μm^2. Dividing the surface area of the Transwell filter by the area of one image at one vertical position, gives 92,244 image regions per Transwell filter. Before pressure application, the LIS area per image is approximately 100 μm^2, which is equivalent to 0.092 cm^2 for the whole filter. With a cell layer height of 20 μm the intercellular volume is approximately 0.00018 cm^3. After pressure application, the LIS area per slice is an average of 500 μm^2. An average cell layer height of 17 μm correlates to an intercellular volume of 0.00078 cm^3. The change in volume, ΔV_{LIS}, is then 0.0005 cm^3.

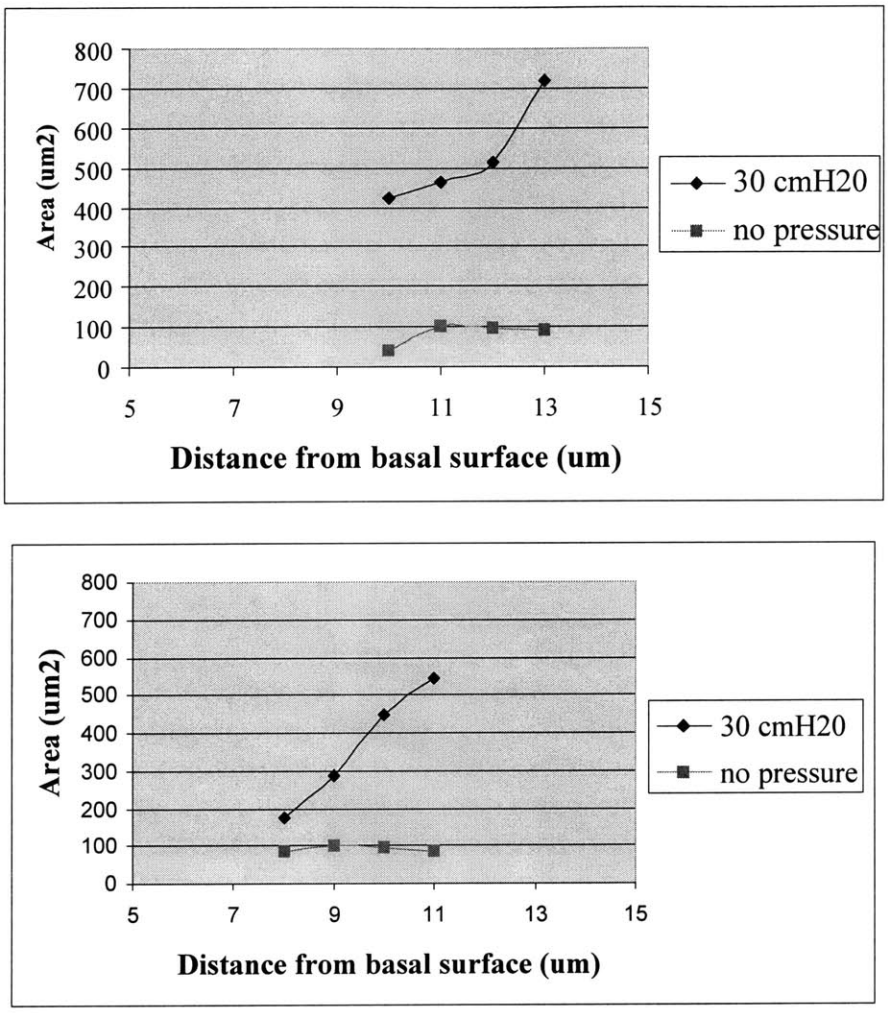

Figure 4.13: Average LIS area for two image pairs measured with Scion Image.

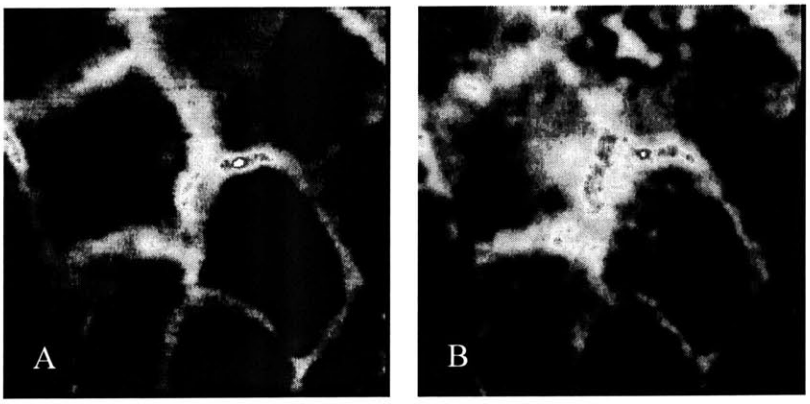

Figure 4.14: BCECF stained cells. A) Before pressure application intercellular spaces and cells are visible. B) During pressure application. A large pool can be seen at the intersection of three cells.

4.3.6.5 Estimation of Net Fluid Transport

The volume flow, J_v, across the cell layer can be calculated from the following equation.

$$J_v = P_f S V_W \Delta[\pi]$$

The osmotic permeability, P_f^A, of the apical surface of airway epithelial cells was determined to be 86.5 ± 24.3 μm/s using confocal microscopy (30). The osmotic permeability of the basolateral surfaces was much smaller than that of the apical surface ($P_f^B << P_f^A$). We assumed P_f^B to be approximately 1 μm/s. V, the partial molal volume of water is 0.018 cm^3/mM, $\Delta[\pi]^B$, the osmotic concentration, is 1.15mOm/L, which is equivalent to the pressure difference of 30 cmH_2O, and S is the surface area through which the volume flux occurs. Figure 4.15 represents the cell layer grown on a porous substrate.

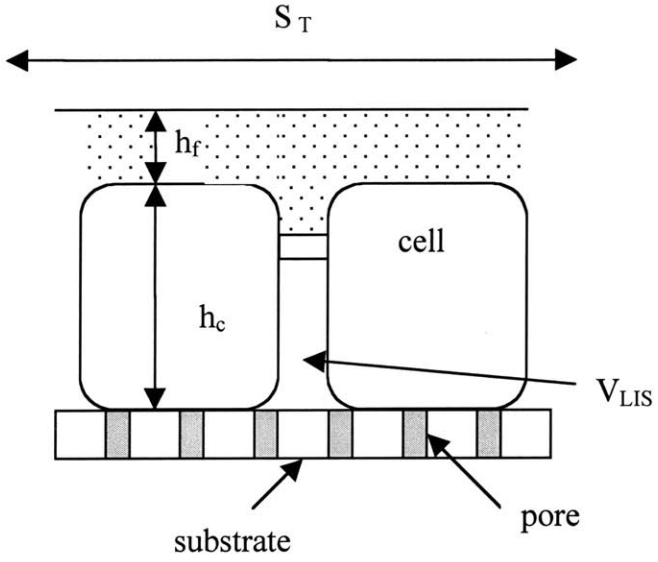

Figure 4.15: Cell layer grown on porous Transwell tissue inserts. S_T is the surface area of the Transwell tissue insert, V_{LIS} is the volume of the intercellular space, V_L is the volume of the liquid layer on top of the cells, h_F is the height of the liquid layer, V_C is the volume of a cells and h_C is the height of the cells. The porous substrate layer is also noted.

S_T, the apical surface area of the cells, is 1.13 cm^2 for 12 mm diameter Transwell filters. If the imposed pressure gradient of 30 cmH_2O occurred entirely across the apical surface,

the fluid volume transported across the apical membrane in one half hour would be 0.364 cm^3.

If the pores are plugged, then fluid could only leave the cell layer through the membrane at the pores. Since there are 4 x 10^6 pores/cm^2 in the Transwell filters, and each pore has a diameter of 0.4 μm, the total surface area for all the pores is 0.005 cm^2. The fluid transported across the membrane at the pores in 30 minutes would then be 1.86 x 10^{-5} cm^3. The rest of the fluid would theoretically leave the cells through the basolateral membranes and would be trapped in the intercellular spaces. Total fluid exchange across the basolateral membrane, J_v^B, indicates how much fluid could be trapped in the LIS after on half hour. Approximately 50,000 cells are plated on each Transwell insert and each cell is approximately cubic with 20 μm sides, giving an basolateral surface area of approximately 1.9 μm^2. J_v^B, would then be 0.007 cm^3.

Using the conservation of mass, the amount of fluid through the basolateral membrane should be equivalent to the volume change of the liquid above the cells, ΔV_L, plus the cell volume change, ΔV_{cell}. ΔV_L can be calculated as follows.

$$V_L = A_T h_L$$
$$\Delta V_L = A_T \Delta h_L$$

Δh_L was determined in a previous section and is approximately -6 μm. Then ΔV_L is -0.0038 cm^3. The LIS volume change, ΔV_{LIS}, also determined in a previous section, is 0.0005 cm^3. The volume change of the cell layer, ΔV_{cell}, can be determined from the following relationships.

$$h_c A_T - V_{LIS} = V_{cekk}$$
$$\Delta V_{cell} = A_T \Delta h_c - \Delta V_{LIS}$$

Using the above values, ΔV_{cell} is –0.00011 cm^3.

J_v^B, the volume of liquid passing through the basolateral membrane of the cells, and J_v^P, the volume of liquid passing through the pores, can be determine from the following equations based on the conservation of mass, and compared to the previous results based on osmotic permeability.

$$J_v^B = -(\Delta V_L + \Delta V_{cell}) = 0.00039 cm^3$$
$$J_v^P = -(\Delta V_L + \Delta V_{cekk} + \Delta V_{LIS}) = 0.00034 cm^3$$

0.00039 cm^3 is well within the range that can pass through the basolateral membrane in one half hour based on the osmotic permeability of the basolateral membrane. However, the value for ΔV_{LIS} shows that only a small amount of fluid was actually trapped in the intercellular spaces during pressurization. The rest of the volume flow, 0.00034 cm^3, presumably leaves the cell layer via the pores in the substrate. This value is much larger that the 1.86×10^{-5} cm^3 that could pass through the membrane at the pores.

In summary, it is feasible that a fluid loss associated with the change in cell layer height occurred through the basolateral walls. However, the change in LIS width does not account for the entire volume flow through the basolateral walls. It is possible that only some of the substrate pores were plugged due to pressure application and that some pores were only slightly impeded allowing some fluid to leave, but trapping the rest in the intercellular spaces. Accumulating fluid would subsequently cause the lateral intercellular spaces to extend. In addition, increased pooling, and larger intercellular spaces near the basal surface, could have contributed to an underestimate of the LIS volume.

4.3.7 Sources of Artifacts

Several possible events could have affected the two-photon imaging results. For example, it is possible that some of the dextran molecules diffused into the cells and made the intercellular spaces look artificially wide. On one hand we showed that 10,000 MW dextran enters the cells and stains the nuclei while the 70,000 MW dextran molecules did not. However, it is possible that some 70,000 MW dextran diffused across the membrane near the LIS and altered the results. Comparing results for cells imaged twice in a row without pressure would be useful for comparing progressive diffusion

Evaporation from the surface of the cell layer is another potential artifact. When the cells differentiate into the pseudostratified layer they produce an air liquid interface that consists of a thin layer of mucus on the apical surface of the cells that keeps the cells moist. Evaporation through prolonged exposure to light and heat when imaging could increase the concentration of salts on the surface of the cells and alter the osmotic balance. When the cells are incubated, they are bilaterally exposed to the dextran or Calcein, AM solutions. After incubation, most of the solution is removed from the apical surface, but a small amount remains. The solution on the surface should prevent the apical surface from drying out. There was no additional fluid on top of the cells when

they were pressurized in the cell culture experiments, so this imaging experiment does replicate the *in vitro* system used previously to investigate a biological response. If evaporation occurred in the imaging tests, it might also have occur in the cell culture experiments.

The placement of the Transwell filter could also contribute to inaccurate results. When the cells are pressurized for immunoblotting experiments the Transwell filter is suspended in a well plate, and the basal surface of the cell layer remains at atmospheric condition. Alternatively, for imaging the Transwell filter is placed directly on a glass cover slip, with only a bolus of fluid separating them. With a transcellular pressure difference the substrate and the cell layer move downward and could effectively create a seal. If the basal surface of the cells is sealed then a) fluid could not exit the cell layer, and b) the pressure difference would be changed.

The fluid bolus was placed between the cover slip and the cells allow the dye to continue to diffuse into the cell layer throughout imaging and to prevent dye from leaking out. However, increased diffusion may also account for the increase in intensity seen in pressurized cells that are in contact with the dye for a longer period of time.

Finally, when the cells are ready to be stained they are removed from their media and from the 37°C incubator. Prolonged lack of nutrients, along with a non-physiologic temperature, may contribute to alterations in the cell layer, including cell death.

4.3.8 Discussion of Two-Photon Results

Imaging studies were performed to determine the effects of a transcellular pressure difference on a pseudostratified layer of airway epithelial cells. Two-photon microscopy allowed live cells to be imaged before and during pressure application, in order to determine if intercellular space widths decreased or if a volume change occurred, and to determine if increased fluid flow in the intercellular spaces was a possible mechanism for mechanotransduction. Both LIS width and area increased, suggesting that the fluid may be inhibited from leaving the cell layer at the pores.

If fluid cannot enter at the tight junctions or exit through the substrate, then shear stress caused by increased fluid flow in the intercellular LIS is unlikely, but cannot be ruled out. It has been shown that the intercellular space in epithelial cells does not act as a fluid channel, but as a dynamic fluid bed where water enters from the cells. The primary

water transport system, the Na^+, K^+ ATPase, is distributed along the length of the intercellular spaces (27) allowing fluid to enter from all sides. If enough fluid enters through the lateral walls and can exit through the basal opening of the LIS, increased shear stress could occur.

Pressurizing the cell layer would cause a pressure gradient in the intercellular space, which would increase osmosis of fluid from the cells to the intercellular spaces. Theoretically, increased water in the LIS would increase the fluid flux across the epithelium by drawing more water out of the cell layer. However, plugs in the porous membrane would limit the out flow of water, again increasing the fluid pools in between the epithelial cells.

These data also show that the cell layer is compressed due to pressure application. The combination of a decrease in cell layer thickness, along with an increase in the width of the intercellular spaces suggests a reduction in epithelial cell volume. It has been shown that the pathways for upregulation of extracellular related kinase (ERK), a mechanically responsive early gene, are different for airway epithelial cells exposed to a transcellular pressure difference and those that are osmotically shocked and subsequently change volume (unpublished results). However, the pathways by which pressure and osmotic stress activate MAP kinases are still unclear.

While results presented here show that a transcellular pressure difference increased LIS widths and decreased cells heights, further studies must be performed to verify the methods and the results. If the results presented here are correct and the intercellular spaces do increase because of trapped fluid, how the increase in width initiates a mechanotransduction cascade is still unknown.

Chapter 5
Summary and Future Work

5.1 Summary

In this thesis, we have shown that the means by which cells respond to their environment is complex and that mechanical stimulation can lead to a biological response through a variety of pathways. Airway epithelial cells in asthmatic airways experience a level of force and a milieu of chemical signals that are absent in normal airways. Based on previous studies, it is likely that these chemical and mechanical signals contribute to the initiation and progression of asthma pathogenesis (10, 37).

Ressler (37) showed that exposing a pseudostratified layer of airway epithelial cells to a transcellular pressure difference upregulation stress activated Egr-1, which is implicated in airway remodeling. We took Ressler's results to the next level and determined that Egr-1 is upregulated through the MAP kinase ERK in response to pressure application. Osmotic shock activated other MAP kinases, including JNK and p38, showing different mechanosensory pathways for pressure and for osmotic challenge. These results give evidence that a transcellular pressure initiates a biological response in airway epithelial cells that is distinct from the response due to osmotic pressure.

A finite element model of an airway epithelial cell on a porous substrate was constructed and used to analyze the stress distribution in response to a transcellular pressure difference. The finite element model of a pressurized cell showed that increased membrane and cytoskeletal stresses occur in the vicinity of the 0.4 μm pores due, in part, to the deformation of the cell into the porous substrate. Increased membrane strains of more than 500 kPa may cause the dissociation of proteins that attach the basal membrane of the cell to the porous substrate and cause active cell movement into the pore. Previous magnetic cytometry results show that transmembrane integrins have the capability to initiate a structural rearrangement of the cytoskeleton that could potentially lead to a biological response. The maximum effective stress in a magnetic cytometry finite element model is an order of magnitude higher than the maximum effective stress in the pressurized cells, although large strains may lead to inaccuracies near the bead.

Increased membrane strain in each of the models may stimulate stress activated ion channels initiating intracellular signaling cascades and stresses in the nucleus may act to

increase transcription of certain proteins. All the models reveal increased stresses in the nucleus, which is stiffer than the cytoskeleton.

A finite element model of two cells separated by an intercellular space indicated that the intercellular spaces may collapse when the cells are pressurized, which would increase shear stress along the walls of the LIS. However, imaging results showed that the intercellular spaces do not collapse as the finite element model suggests, but may actually increase. Mechanosensory pathways that involve volume change and fluid transport across both the cell membrane and the substrate may play a leading role in initiating a biological response.

Osmotic shock to a membrane causes water to move across the concentration gradient. Therefore, and increase in osmotic pressure in the LIS would cause water to move across the lateral membrane to restore equilibrium. Fluid transport across the lateral membrane and into the LIS would increase the volume of the intercellular spaces and could increase strains in the lateral membranes due to the swelling. Together water transport and membrane strain could activate different MAP kinase family members than an osmotic shock acting along at the basal membrane.

It is likely that many mechanisms are at work in the signaling system of airway epithelial cells exposed to a transcellular pressure difference. This thesis attempted to take a closer look at the magnitude and location of stresses and strains induced by pressure application in order to determine where mechanotransduction may occur and by what pathways. Previous studies ruled out substrate strain, hydrostatic pressure, and osmotic shock through the porous substrate. The results from this study show that a volume change may occur along with an increase in the width of the intercellular spaces. Further tests need to be performed in order to determine if fluid flow is passive, if it is controlled by ion channels, if the cells have the capability to plug the pores in the substrate, and if the viability of the cells decreased due to prolonged imaging time.

If the pores are indeed plugged by the increased pressure, or if the cells dried out, then a question remains as to how accurately this cell culture system represents the *in vivo* system. In the original *in vitro* system, the airway epithelial cells were grown on a fibrous collagen mesh. Upregulation of Egr-1 was the same when the cells were grown on the collagen mesh as it was when the cells were grown on polyester porous substrates.

Even if the pores are plugged in this study, it is unlikely that the phenomenon is acting alone as the mechanosensory mechanism.

5.2 Future Work

The work presented in this thesis addresses issues that were raised in previous studies, and suggests new avenues to pursue in determining mechanotransduction pathways. One of the next steps in this study is to verify the imaging results and to determine if increased diffusion of dextran molecules over time enhances the intensity in the intercellular spaces leading to artificial dimensions. In addition, further studies must be performed to determine if the cells are drying out over time and what affect drying out would have on the results. It is also important to determine if the same biological response occurs when the Transwell filter is sitting on a cover slip in the imaging study, as when the Transwell is suspended in a well as it was in the original ERK/Egr-1 studies.

Determining the flux across the cell layer and the osmotic water permeability before and during pressure application would indicate whether or not the pores are being plugged or if pressure affects the fluid flow at all. An increase in water flux would suggest that shear stress in the intercellular spaces is a possibility, that transport across the cell membrane increases, or that the tight junctions are affected.

There is also a question as to whether or not fluid transport across the *in vitro* epithelial cell layer is a dynamic process, controlled by active channels along the apical and basolateral membranes, or if it is passive, with fluid either going through the tight junction, or diffusing passively through pores in the membrane. Active fluid transporting membrane channels have been found along the basolateral membrane of airway epithelial as discussed previously, but their role in this study and their existence in this culture system has not been determined.

Shear stress is a well-studied mechanical stimulus that leads to the activation of MAP kinase family members ERK, JNK, and p38 when the shear stress is applied along the apical surface of a monolayer of cells. For pressurized airway epithelial cells, altered flow patterns in the intercellular spaces may contribute to the activation of ERK. Preliminary test were performed in order to determine if ERK is activated due to fluid flow along the apical surface of a monolayer of airway epithelial cells. Results for two

tests did not show a pattern of activation, although the procedure needs to be reassessed and the tests rerun before the results can be considered conclusive. In addition, the shear stress activation cascade initiated by shear stress on the apical surface may be different from shear stress applied to the basolateral surfaces that do not normally experience high shear stresses. Regardless, information about the activation of ERK due to shear stress in airway epithelial cells will provide additional information that can be compared to the activation of ERK in response to a pressure difference.

Finally, as more information becomes available, the finite-element models can be updated to better represent the physical system. Epithelial cells are highly three-dimensional and the two-dimensional models presented in this study provide a comprehensive, but limited model. A three-dimensional viscoelastic model would provide more accurate information about the locations of increased stresses in pressurized epithelial cells.

This thesis provided another step in determining the role of mechanical forces in cellular systems. For many years medicine and engineering were thought of as entirely separate fields that rarely overlap. However, in the last couple decades increased attention has focused on the significant role that mechanical forces play at the molecular, cellular, and systemic level. It is apparent from this study and others that many complex mechanical forces arise in cellular systems and that they play an active role in the environment in which cells grow and adapt. In this thesis important results regarding signaling pathways, increased stresses, and fluid transport were obtained that point to possible mechanosensory pathways. Future work will expound upon these pathways and provide more building blocks from which to construct a framework for mechanotransduction in airway epithelial cells

Bibliography

1. ADINA *Theory and Modeling Guide*. Vol. 1. ADINA R&D, Inc., Watertown MA. 1997.

2. Bathe, K.J. *Finite Element Procedures*, Prentice Hall Inc., New Jersey: 1996.

3. Bourns, B., Franklin, S., Cassimeris, L., and E.D. Salmon. High hydrostatic pressure effects in vivo: changes in cell morphology, microtubule assembly, and actin organization. *Cell Motil. Cytoskeleton.*10(3): 380-90, 1988.

4. Caille, N., Tardy, Y., and J.J. Meister. Assessment of strain field in endothelial cells subjected to uniaxial deformation of their substrate. *Ann. Biomed. Eng.* 26: 409-416, 1998.

5. Chatton, J.Y., and K.R. Spring. Acidic pH of the lateral intercellular spaces of MDCK cells cultured on permeable supports. *J. Membrane Biol.* 140: 89-99, 1994.

6. Coers, W., Vos, J.T., Huitema, S., Dijk, F., and J.J. Weening. Biological alterations of rat podocytes cultured under basolateral hydrostatic pressure. *Pathobiology*. 64(4): 222-32, 1996.

7. Cohen, D.M., Chin, W.W., and S.R. Gullans. Hyperosmotic urea increases transcription and synthesis of Egr-1 in murine inner medullary collecting duct (mIMCD3) cells. *J. Biol. Chem.* 269(41): 25865-70, 1994.

8. Davies, P.F. Flow-mediated endothelial mechanotransduction. *Physiol. Rev.* 75:519-560, 1995.

9. Dewey, C.F. Effects of fluid flow on living vascular cells. *J. Biomech. Eng.* 106:31-35, 1984.

10. Elias, J.A., Zhu, Z., Chupp, C., and R.J. Homer. Airway remodeling in asthma. *J. Clin. Invest.* 104: 1001-1006, 1999.

11. Evans, E., and A. Yeung. Apparent viscosity and cortical tension of blood granulocytes. *Biophys. J.* 56(1): 151-60, 1989.

12. Felix, J.A., Woodruff, M.L., Dirksen, E.R. Stretch increases inositol 1,4,5-trisphosphate concentration in airway epithelial cells. *Am. J. Respir. Cell Mol. Biol.* 14(3): 296-301, 1996.

13. Filippatos, G.S., Hughes, W.F., Qiao, R., Sznajder, J.I, and B.D. Uhal. Mechanisms of liquid flux across pulmonary alveolar epithelial cell monolayers. *In Vitro Cell. Dev. Biol. – Animal.* 33: 165-200, 1997.

14. Fredericksen, O., and J. Rostgaard. SEM fixation produces artificially dilated spaces. *J. Cell Biol.* 61: 830-833, 1974.

15. Guilak, F., Tedrow, J.R., and R. Burgkart. Viscoelastic properties of the cell nucleus. Biochem. Biophys. Res. Commun. 269(3): 781-786, 2000.

16. Gunst, S.J., and J.Q. Stropp. Pressure-volume and length-stress relationships in canine bronchi in vitro. *J. Appl. Physiol.* 64: 2522-2531, 1998.

17. Harrigan, T.P., Jasty, M., Mann, R.W., and W.H. Harris. Limitations of the continuum assumption in cancellous bone. *J Biomech.* 21(4): 269-75, 1998.

18. Hwang, W.C., and R.E. Waugh, R.E. Energy of dissociation of lipid bilayers from the membrane skeleton of red blood cells. *Biophys. J.* 72(6): 2669-78, 1997.

19. Ishida, T., Peterson, T.E., Kovach, N.L., and B.C. Berk. MAP kinase activation by flow in endothelial cells. Role of beta 1 integrins and tyrosine kinases. *Circ Res.* 79(2): 310-6, 1996.

20. Itoh, T., Yamauchi, A., Miyai, A., Yokoyama, K., Kamada, T., Ueda, N., and Y. Fujiwara. Mitogen-activated protein kinase and its activator are regulated by hypertonic stress in Madin-Darby canine kidney cells. *J. Clin. Invest.* 93(6): 2387-92, 1994.

21. Jacoby, D.B. Role of the respiratory epithelium in asthma., 68th Forum in Immunology, pp 48-58, 1996.

22. James, A.J. Relationship between airway wall thickness and airway hyperresponsiveness, *in Airway Wall Remodeling in Asthma.* A.G. Sterwart, editor. CRC Press, Boca Raton, FL. 1-27, 1997.

23. Janmey, P.A. Mechanical properties of cytoskeleton polymers. *Curr. Op. Cell Biol.* 2:4-11, 1991.

24. Khachigian, L.M., Williams, A.J., and T. Collins. Interplay of Sp1 and Egr-1 in the proximal platelet–derived growth factor A-chain promoter in cultured vascular endothelial cells. *J. Biol. Chem.* 270: 27679-27686, 1995.

25. Kim, Y.K., Dirksen, E.R., and M.J. Sanderson. Stretch-activated channels in airway epithelial cells. *Am. J. Physiol.* 265(5 Pt 1): C1306-18, 1993.

26. Kovbasnjuk, O., Leaser, J.P., Weinstein, A.M., and K.R. Spring. Water does not flow across the tight junctions of MDCK cell epithelium. *Proc. Natl. Acad. Sci.* 95: 6526-6530, 1998.

27. Kyte, J. Immunoferritin determination of the distribution of (Na^+ + K^+) ATPase over the plasma membranes of renal convoluted tubules. II. Proximal segment. *J. Cell. Biol.* 69: 304-18, 1976.

28. Lee, H.S., Millward-Sadler, S.J., Wright, M.O., Nuki, G., and D.M. Salter. Integrin and mechanosensitive ion channel-dependent tyrosine phosphorylation of focal adhesion proteins and beta-catenin in human articular chondrocytes after mechanical stimulation. *J. Bone Miner. Res.* 15(8): 1501-9, 2000.

29. Lodish, H., Berk, A., Zipursky, S.L., Matsudaira, P., Baltimore, D., and J. Darnell. *Molecular Cell Biology.* 4th ed. New York: W.H. Freedman and Co., 2000.

30. Matsui, H., Davis, C.W., Tarran, R., and R.C. Boucher. Osmotic water permeabilities of cultured, well-differentiated normal and cystic fibrosis airway epithelia. *J. Clin. Invest.* 105(10): 1419-1427, 2000.

31. Needham, D., and R.S. Nunn. Elastic deformation and failure of lipid bilayer membranes containing cholesterol. *Biophys. J.* 58(4): 997-1009, 1990.

32. Niisato, N., Post, M., Van Driessche, W., and Y. Marunaka. Cell swelling activates stress-activated protein kinases, p38 MAP kinase and JNK, in renal epithelial A6 cells. *Biochem. Biophys. Res. Commun.* 266(2): 547-50, 1999.

33. Ogata, T. Fluid flow-induced tyrosine phosphorylation and participation of growth factor signaling pathway in osteoblast-like cells. *J. Cell Biochem.* 76(4): 529-38, 2000.

34. Paul, W.E. Interleukin 4: Signaling mechanisms and control of T cell differentiation. *Ciba Foundation Symposia.* 204: 208-216, 1997.

35. Potard U.S.B., Butler, J.P., and N. Wang. Cytoskeletal mechanics in confluent epithelial cells probed through integrins and E-cadherins. *Am. J. Physiol.* 272: C1654-C1663, 1997.

36. Raeburn, D., and S.E. Webber. Proinflammatory potential of the airway epithelium in bronchial asthma. *Eur. Respir. J.* 7: 226-233, 1994.

37. Ressler, B., Lee, R.T., Randell, S.H., Drazen, J.M., and R.D. Kamm. Molecular responses of rat tracheal epithelial cells to transmembrane pressure. *Am. J. Physiol. Lung. Cell Mol. Physiol.* 278: L1264-L-1272, 2000.

38. Reusch, H.P., Chan, G., Ives, H.E., and R.A. Nemenoff. Activation of JNK/SAPK and ERK by mechanical strain in vascular smooth muscle cells depends on extracellular matrix composition. *Biochem. Biophys. Res. Commun.* 237(2): 239-44, 1997.

39. Reuss, L., Vanoye, C.A., Altenberg, G.A., Vergara, L. Subramaniam, M., and R. Torres. Cell-volume changes and ion conductances in amphibian gallbladder epithelium. *Cell Physiol. Biochem.* 10(5-6): 385-392, 2000.

40. Satcher, R.L., Dewey, C.F., and J.H. Hartwig. Mechanical remodeling of the endothelial surface and actin cytoskeleton induced by fluid flow. *Microcir.* 4: 439-453, 1997.

41. Sato, M., Oshima, N., and R.M. Nerem. Viscoelastic properties of cultured porcine aortic endothelila cells exposed to shear stress. J. Biomech. 29(4): 461-7. 1996.

42. Savla, U., and C.M. Waters. Mechanical strain inhibits repair of airway epithelium in vitro. *Am. J. Physiol.* 274(6 Pt 1): L883-92, 1998.

43. Savla, U., Sporn, P.H., and C.M. Waters. Cyclic stretch of airway epithelium inhibits prostanoid synthesis. *Am. J. Physiol.* 273(5 Pt 1): L1013-9, 1997.

44. Schwachtgen, J.L., Houston, P., Campbell, C., Sukhatme, V., and M. Braddock. Fluid shear stress activation of egr-1 transcription in cultured human endothelial and epithelial cells is mediated via the extracellular signal-related kinase 1/2 mitogen-activated protein pathway. *J. Clin. Invest.* 101(11): 2540-9, 1998.

45. Schwartz, L.B. Cellular inflammation in asthma: neutral proteases of mast cells. *Am. Rev. Respir. Dis.* 145 (2 Pt 2): S18-21, 1992.

46. Skalak, R., Dong, C., and C. Zhu. Passive deformations and active motions of leukocytes. *J. Biomech. Eng.* 112: 295-302, 1990.

47. So, P.T., Kim, H., and I.E. Kochevar. Two-photon deep tissue ex vivo imaging of mouse dermal and subcutaneous structures. *Optics Express* 3: 339-351, 1998.

48. Spring, K. Epithelial fluid transport – A century of investigation. *News Physiol. Sci.* 14: 92-98, 1999.

49. Spring, K.R. Routes and mechanism of fluid transport by epithelial. *Ann. Rev. Physiol.* 60: 105-119, 1999.

50. Spring, K.R., and A. Hope. Size and shape of the lateral intercellular spaces in a living epithelium. Science 200: 54-58, 1978.

51. Stamenovic, D., and N. Wang. Cellular responses to mechanical stress. Invited Review: Engineering approaches to cytoskeletal mechanics. *J. Appl. Physiol.* 89: 2085-2090, 2000.

52. Sumpio, B.E., and A.J. Barnes. Response of porcine aortic smooth muscle cells to cyclic tensional deformation in culture. *J. Surg. Res.* 44(6): 696-701, 1988.

53. Takahashi, M., Ishida, T., Traub, O., Corson, M.A., and B.C. Berk. Mechanotransduction in endothelial cells: temporal signaling events in response to shear stress. *J. Vasc. Res.* 34(3): 212-9, 1997.

54. Tarbell, J.M., Lucas, D., and M.M. Zaw. Effect of pressure on hydraulic conductivity of endothelial monolayers: role of endothelial cleft shear stress. *J. Appl. Physiol.* 87(1): 261-268, 1999.

55. Theret, D.P., Levesque, M.J., Sato, M., Nerem R.M., and L.T. Wheeler. The application of a homogeneous half-space model in the analysis of endothelial cell micropipette measurements. *J. Biomech. Eng.* 110: 190-199, 1998.

56. Tsay, R.-Y., and S. Weinbaum. Viscous flow in a channel with periodic cross-bridging fibres: exact solutions and Brinkman approximation. *J. Fluid Mech.* 226, 125 –148, 1991.

57. Wang, N., and D.E. Ingber. Control of cytoskeletal mechanics by extracellular matrix, cell shape, and mechanical tension. *Biophys. J.*, 66: 2181-2189, 1994.

58. Wang, N., Butler, J.P., and D.E. Ingber. Mechanotransduction across the cell surface and through the cytoskeleton. *Science.* 260: 1124-1127, 1993.

59. Ward, M.D., and D.A. Hammer. A theoretical analysis for the effect of focal contact formation on cell-substrate attachment strength. *Biophys, J.* 64(3): 936-59, 1993.

60. Weinberger, S.E. *Principles of Pulmonary Medicine*. Philadelphia, PA: Saunders, 1992, p 72-86.

61. Wiggs, B.R., Hrousis, C.A., Drazen, J.M., and R.D. Kamm. On the mechanism of mucosal folding in normal and asthmatic airways. *J. Appl. Physiol.* 83: 1814-1821, 1997.

62. Woolley, K.L., Adelroth, E., Woolley, M.J., Ellis, R., Jordana, M., and P.M. Obyrne. Effects of allergen challenge on eosinophils, eosinophil cationic protein, and granulocyte-macrophage colony–stimulating factor in mild asthma. *Am. J. Repir. Crit. Care Med.* 151: 1915-1924, 1995.

63. Wung, B.S., Cheng, J.J., Chao, Y.J., Hsieh, H.J., and D.L. Wang. Modulation of Ras/Raf/extracellular signal-regulated kinase pathway by reactive oxygen species is involved in cyclic strain-induced early growth response-1 gene expression in endothelial cells. *Circ. Res.* 84(7): 804-12, 1999.

64. Yeager, D., Martins, M.A., Feldman, H., and R.D. Kamm. Acute histamine-induces flux of airway liquid: role of neuropeptides. *J. Appl. Physiol.* 80: 1285 –1295, 1995.